Effects of ambient viscosity on the entrainment and dynamics of a buoyant jet

A thesis

submitted for the degree of

MASTER OF SCIENCE (ENGINEERING)

by

MANIKANDAN M.S.

ENGINEERING MECHANICS UNIT
JAWAHARLAL NEHRU CENTRE FOR ADVANCED
SCIENTIFIC RESEARCH
BANGALORE - 560064

AUGUST 2005

DECLARATION

I hereby declare that the work embodied in the thesis entitled "**Effects of ambient viscosity on the entrainment and dynamics of a buoyant jet**" is the result of investigations carried out by me at the Engineering Mechanics Unit, Jawaharlal Nehru Centre for Advanced Scientific Research, Bangalore, India under the supervision of Dr. K.R. Sreenivas and that it has not been submitted elsewhere for the award of any degree or diploma.

In keeping with the general practice in reporting scientific observations, due acknowledgement has been made whenever the work described is based on the findings of other investigators.

M.S. Manikandan

CERTIFICATE

I hereby certify that the work embodied in this thesis entitled "**Effects of ambient viscosity on the entrainment and dynamics of a buoyant jet**" has been carried out by Mr. M.S. Manikandan at the Engineering Mechanics Unit, Jawaharlal Nehru Centre for *Advanced Scientific Research, Bangalore, India under my supervision and that it has not* been submitted elsewhere for the award of any degree or diploma.

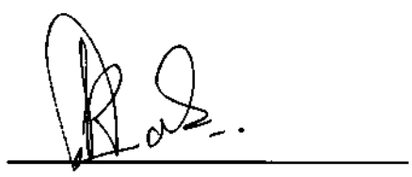

Dr. K.R. Sreenivas
(Research Supervisor)

Acknowledgements

I would like to sincerely acknowledge Dr. K.R.Sreenivas for his guidance throughout my work. I especially thank him for allowing me to continue working on the problem that I had started working on, as a summer student.

I also would like to thank Prof. Rama Govindarajan for her constant support and encouragement. Her suggestions at various stages of my work have been very helpful. A big thanks to Prof. Roddam Narasimha for his valuable suggestions and comments during my seminars.

Mukund's help in my project has been invaluable. I sincerely thank him for his time and effort in helping me out in my experiments. Discussions with him have also been very inspiring. Thanks to Shreyas in assisting me at various stages in the experiments. Mukund and Shreyas have been absolutely fantastic lab mates to live with.

I also would like to thank Faraz for his help during the initial stages. Sincere acknowledgements to Vinod and Sameen for teaching me to work with "Linux". Thanks are due to Aneesh, Punit, Kaushik, Pinaki, Kirti and Anjana.

I am grateful to JNCASR for giving me an opportunity to work here for my M.S. Mr. Arokianathan at the workshop has been absolutely great whenever I have approached him for help. Thanks to all the people at Dr. Ranga Uday's lab for letting me use their camera at various points in time.

I also would like to acknowledge my parents and my brother for their constant support and encouragement.

Synopsis

A free-shear flow driven by both initial momentum and buoyancy is a buoyant jet. Turbulent buoyant jets spread in a direction normal to their primary-flow direction by incorporating irrotational ambient fluid into the turbulent jet-flow; this process is known as entrainment. Entrainment process and hence the dynamical behavior of the jet depend on several parameters such as ambient density stratification, axial-pressure gradient, cross-flow and off-source buoyancy addition, temperature and viscosity contrasts between the free-shear flow and the ambient medium.

In this thesis, the effects of the viscosity of the ambient fluid on the entrainment and dynamics of a buoyant jet are studied via experiments and 2-D simulations using vortex methods. Some of the applications of the above situation include the flow of lava into a magma chamber, where viscosity variation arises due to a change in temperature and/or constituents, and the process industry where polymers have to be blended with additives or with polymers having different physical properties.

All the experiments are conducted in a glass tank of dimensions 30x30x45 cm^3. A buoyant jet issuing into a fluid of viscosity different from that of the jet fluid (viscosity enhanced by addition of suitable amounts of Sodium carboxymethyl cellulose) is studied using flow-visualization and other entrainment-quantification experiments. Experimental results indicate that the turbulent jet undergoes a reverse transition. Large scale eddies at the interface are suppressed, and the observed entrainment rate also reduces dramatically for the jet in a higher-viscosity medium.

Results from 2-D numerical simulations, using vortex methods are also presented. Issues concerning viscosity-stratification in vortex methods are addressed. Results from the numerical simulations have a reasonable agreement with the experimental results.

CONTENTS

Chapter 1

1. Introduction

1.1 Free-Shear flows

An unbounded region of a large body of fluid that either has an excess momentum (a jet or a plume for example) or a momentum deficit (a wake for example) is a free-shear flow. Various types of free-shear flows that are observed in nature are jets (driven by initial momentum), plumes (driven by initial buoyancy), wakes (characterized by initial momentum deficit) and a mixing layer (characterized by a velocity difference across the interface between two co-flowing fluids).

Typical pictures exhibiting the behavior of various free-shear flows are shown in figure 1.1. (Blue curves indicating the corresponding velocity profiles)

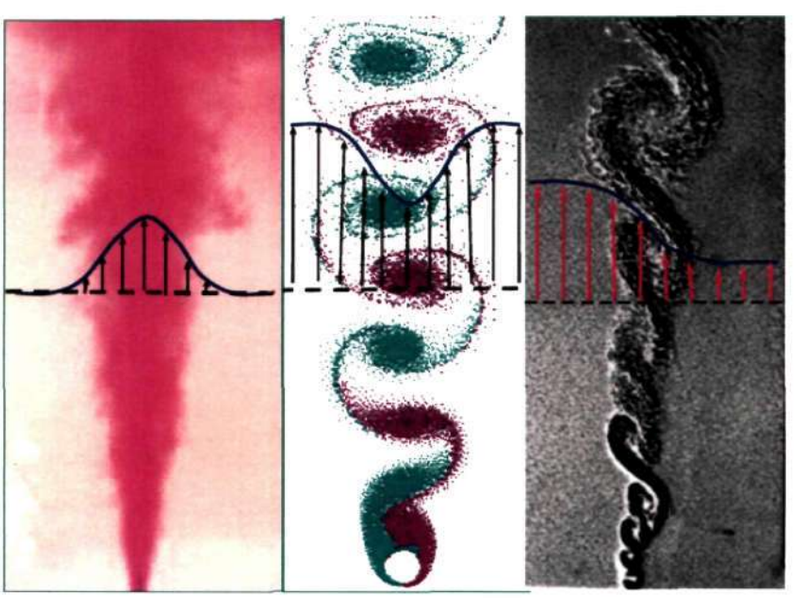

a) JET/PLUME (Experiment) **b)** WAKE (Simulation) **c)** MIXING LAYER (Experiment)

Figure 1.1: Free-shear flows

A free-shear flow, developing in the downstream direction induces the irrotational ambient fluid to get into and mix with the turbulent main flow. This process of bringing in ambient fluid into the free-shear flow and mixing with it is known as **entrainment**.

Free-shear flows and associated entrainment processes are observed in natural phenomena like rising of cumulus clouds, smoke coming out of a chimney and a volcanic plume. Such flows encountered in most of the natural phenomena and other circumstances are invariably turbulent as the laminar counterparts in free-shear flows become unstable at moderately low Reynolds numbers. The fact that free-shear flows in most practical situations are turbulent and that, only laminar flows can be analytically studied, makes the study of turbulent entrainment even more interesting.

Controlling the mixing of the jet (or plume) with its surroundings is a focus of active research. Typical engineering applications demand enhanced combustion between injected fuel and background oxidizer, rapid initial mixing and submergence of effluent fluid, or improved mixing of a hot exhaust with the surroundings. In this context, there is a crucial interest in recognizing and understanding the local nature of the jet instabilities and their global nonlinear development in space and time. On the other hand, purely academic research in this area is also exciting since it deals with the many challenging unresolved scientific issues of non-linear fluid dynamics and turbulence.

The entrainment process in jets and plumes are well studied and literature on this topic dates back to the seminal paper by Morton, Taylor and Turner [1]. Entrainment in free-shear flows is affected by buoyancy at source [1,2], off-source volumetric heating [3], pressure gradient [4,5], axial acceleration (e.g. by external magnetic field) [6] and non-circularity of the jets [7]. Another factor that could possibly affect the entrainment process is the viscosity of the ambient fluid. Campbell and Turner [8] have conducted preliminary studies and given qualitative results on the effects of viscosity differences between the jet and the ambient fluid on the entrainment process. In this work, we have primarily studied the role that the viscosity of the ambient fluid plays in the entrainment process in a buoyant jet.

1.2 Turner's work: An Overview [1, 2, 9]

The entrainment hypothesis in its original form can be stated very simply: "the mean inflow velocity across the edge of a turbulent flow is assumed to be proportional to a characteristic velocity, usually the local time-averaged maximum mean velocity or the mean velocity over the cross-section at the level of inflow". The total inflow at any position will depend also on the surface area and the geometry and dynamics of the flow – whether it is axisymmetric or two-dimensional, a continuous jet or plume or a suddenly released 'thermal'. In this form the assumption is deceptively simple, and even obvious, since for a jet in uniform surroundings it can be deduced from the similarity solution or justified by the most elementary dimensional considerations, as shown in the next section. It has been enormously successful when applied to phenomena over a very wide range of Reynolds numbers, from laboratory scale experiments to geophysical ones like the volcanic plumes.

The entrainment assumption, relating the inflow velocity to the local mean velocity of a turbulent flow, is used successfully to describe natural phenomena over a wide range of scales. Sir Geoffrey Taylor first introduced the entrainment hypothesis in a wartime report on the dynamics of hot gases rising in air. He spoke about it later at a Pacific Science Association meeting in 1949, but did not follow up that talk with a published paper. The idea received a wider exposure through the review lecture by Batchelor (1954) and was formally published by Morton B.R. et. al.[1]

1.2.1 Jets and plumes in a homogeneous environment[2]

Only steady flows in jets and plumes are treated here. The three basic integral properties of these flows (integrated across the cross-sectional area at any level) are the fluxes of mass, momentum and buoyancy. These are defined by:

$$\rho\mu = 2\pi \int_0^\infty \rho w r dr , \qquad (1.1)$$

where **μ** is the 'specific mass flux' or volume flux, and w is the local mean vertical velocity at radius **r** from the vertical line above the source (figure 1.2);

$$\rho m = 2\pi \int_0^\infty \rho w^2 r dr , \tag{1.2}$$

where **m** is the specific momentum flux; and

$$\rho\beta = 2\pi \int_0^\infty \rho w g' r dr , \tag{1.3}$$

where **β** is the specific buoyancy flux and $g' = g\Delta\rho / \rho_0$, the effective gravitational acceleration, and ρ_0 is the constant density of the environment.

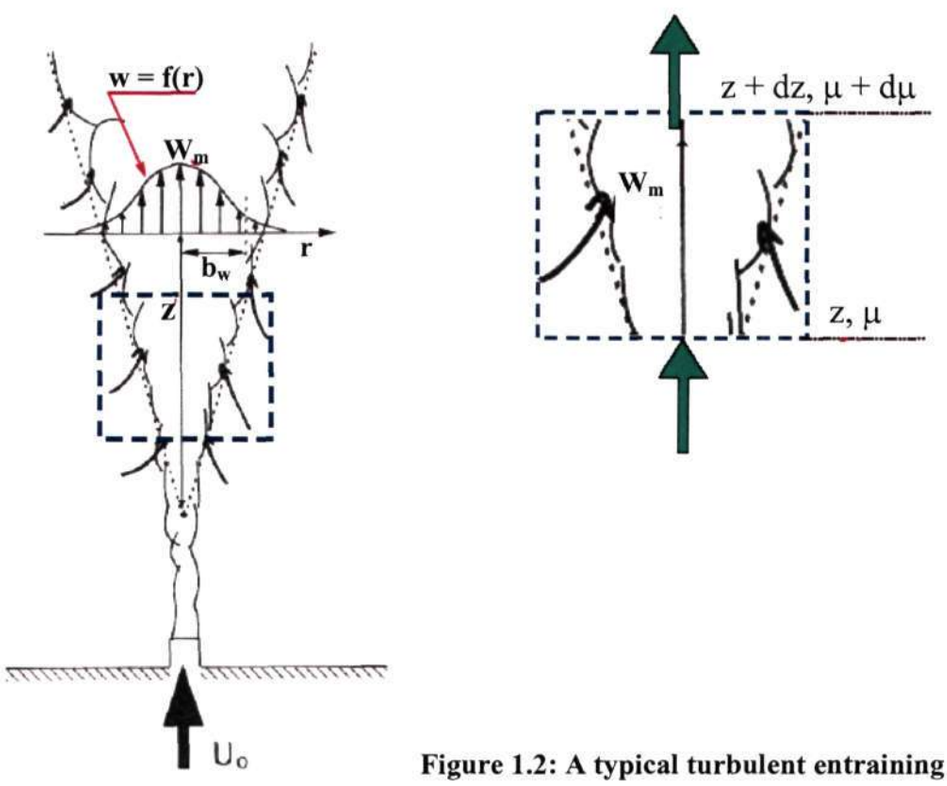

Figure 1.2: A typical turbulent entraining jet

Figure 1.2 depicts the axial velocity profile in a turbulent jet/plume and also explains what we refer to as '**entrainment**', which results in an increased axial mass flow at any axial location.

The symbols **Q, M and B** are used to denote the initial values of μ, **m and** β. These three are the primary variables governing the behaviour of axisymmetric turbulent buoyant jets provided that the Reynolds number $M^{1/2}/\nu$ exceeds a few thousand, as it does in most cases of geophysical interest. When the characteristic linear dimension of the source is small compared with the height of rise, **Q** soon becomes negligible compared with μ and the flow can be treated as if it arose by supplying **M** and/or **B**, but no volume flux, at a point (the virtual source) some distance from the actual source.

The pure jet is defined by **M** alone, since m remains constant at all distances **z**. The mean (time-averaged) velocity is self-similar, and is described well by the Gaussian profiles

$$W = W_m \exp[-(\frac{r}{b_w})^2] \tag{1.4}$$

where $\mathbf{W_m}$ is the mean velocity on the centerline, and $\mathbf{b_w}$ is a radial scale for velocity. The spread of a passive tracer θ (which is assumed now to be so dilute that it has no dynamical effect, though its flux $\mathbf{F_\theta}$ is defined by an integral like (1.3)) is given by

$$\theta = \theta_m \exp[-(\frac{r}{b_\theta})^2] \tag{1.5}$$

Dimensional analysis leads immediately to the following forms for the variation of $\mathbf{W_m}$, θ_m, $\mathbf{b_w}$ and $\mathbf{b_\theta}$ with the overall parameters **M** and **z** (the similarity solution):

$$\left.\begin{aligned} W_m &= k_1 M^{\frac{1}{2}} z^{-1} \\ \theta_m &= k_2 F_\theta M^{-\frac{1}{2}} z^{-1} \\ b_w &= 0.107 z \\ b_\theta &= 0.126 z \end{aligned}\right] \tag{1.6}$$

where the constants in the last two relations are experimentally determined values. Note that the spreads of both velocity and tracer are conical with distance **z** from the source with, however, a wider spread of tracer relative to velocity. (This result, with the same ratio of $\mathbf{b_\theta/b_w}$, is also a characteristic feature of plumes, in which the 'tracer', for example temperature, is dynamically active.) The conical form follows from the similarity

assumption, regardless of the form of the profiles, but the specific numerical values given in (1.6) do of course depend on the measured profiles (1.4) and (1.5). Measurements of turbulent velocities and tracer-concentration fluctuations show that these also have a self-similar radial distribution, and scale with **M** and **z** in a manner consistent with similarity. The constants $\mathbf{k_1}$ **and** $\mathbf{k_2}$ in (1.6) can be evaluated using the measured profiles (1.4) and (1.5) and the corresponding measurements of turbulence quantities. The value of $\mathbf{k_1}$ computed ignoring the axial turbulent flux of momentum (i.e. assuming that all the momentum is carried entirely by the mean flow) is 7.5, but this is reduced to 6.9 (in better agreement with the values derived directly from (1.6)) if the turbulent flux is included. Similar arguments can be applied to the flux of a conserved tracer to give $\mathbf{k_2}$=5.8; again it has been found that the axial turbulent flux is not zero, and needs to be taken into account to be consistent with the measurements.

It also follows from the definition (1.1) and the similarity solution for the jet (1.6) that

$$(\mu)\alpha(wb^2)\alpha(M^{\frac{1}{2}}z) \tag{1.7a}$$

so that

$$\frac{d\mu}{dz} = C_j M^{\frac{1}{2}} \tag{1.7b}$$

The constant $\mathbf{C_j}$ for the jet has been found from experiments to have a value of about 0.25[10]. The form (1.7a) implies that there is a mean rate of inflow across a circular boundary (at radius $\mathbf{b_w}$, say), which is proportional to $(\mathbf{z})^{-1}$, and therefore proportional to the vertical velocity scale $\mathbf{W_m}$ given by (1.6). Thus in this simple case the entrainment relation does not require an independent assumption, but it follows from the similarity considerations which led to (1.6). Moreover, once attention has been concentrated on the inflow velocity, the argument can be turned around: the relations (1.6) can be regarded as a consequence of the simple dimensional assumption that this 'entrainment velocity' should be proportional to the mean (time-averaged) upward velocity $\mathbf{W_m}$ (which is the sole velocity scale needed if the flow remains similar).

The corresponding results for pure axisymmetric plumes in homogeneous surroundings, in which **B** is the conserved quantity, can now be described succinctly in similar terms. In all cases where **B** is large enough to be of geophysical interest, the flow will become

turbulent at a small distance above the source, and **Q** will be negligible, so that all plume properties will depend on **B** and **z**. Assuming similar mean profiles (which experimentally are again found to be closely Gaussian) leads to a linear spread and the following similarity solutions for the maximum vertical velocity and the density difference on the axis:

$$W_m = c_1 B^{\frac{1}{3}} z^{-\frac{1}{3}}$$
$$g'_m = c_2 B^{\frac{2}{3}} z^{-\frac{5}{3}} \tag{1.8}$$

where c_1 and c_2 are constants. The available measurements of turbulent quantities are far fewer for plumes than jets: in particular the magnitude of the axial turbulent fluxes is still uncertain, and so therefore are the precise values of c_1 and c_2. There is no doubt, however, that the levels of turbulent intensity and of concentration fluctuations are much higher in plumes than in jets[11].

Related dimensional arguments can be used to write the dependence of μ and **m** on **B** and **z**,

$$(m) \alpha (B^{\frac{2}{3}} z^{\frac{4}{3}})$$
$$(\mu) \alpha (B^{\frac{1}{3}} z^{\frac{5}{3}})$$

Both of these are now increasing with **z**, as buoyancy acts to increase the momentum of the flow and entrainment to increase its volume. Eliminating **B** gives

$$\mu = C_p m^{\frac{1}{2}} z \tag{1.9a}$$

where C_p is a constant with an experimentally determined value of 0.25. This is the same relation as obtained earlier for the jet, except that the local momentum flux **m** replaces the constant momentum flux **M** for the jet. Taking into account the dependence of **m** on **z**, it follows that for the plume

$$\frac{d\mu}{dz} = \frac{5}{3} C_p m^{\frac{1}{2}} \tag{1.9b}$$

which should be compared with (1.7b). Thus the rates of entrainment into jets and plumes are both defined by the local specific momentum flux **m**, but (since C_p has the same

numerical values as C_j in (1.7b)), the experimentally determined coefficient of proportionality (or 'entrainment rate') is higher for plumes. As first pointed out by Batchelor[12], it follows from the above that for plumes as well as for jets the entrainment relation is a fundamental consequence of the similarity arguments which predict the linear spread of radius with height, and is not an independent assumption.

In the transition regime between jets and plumes, there will therefore be some uncertainty about the entrainment and dilution rate, though the form of dependence on the integral flow quantities is the same in the two limiting cases. In practical situations, however, the jet-like region is often small. The initial specific momentum flux **M** is continuously being increased by buoyancy, and the buoyancy-generated momentum dominates above a height of order $l_m = M^{\frac{3}{4}} B^{-\frac{1}{2}}$ (Morton[13]). Fischer et. al. [10] have contrasted the behaviour of three flows: a pure jet, a pure plume and a buoyant jet having the same $\mathbf{M} = 3\ m^4\ s^{-2}$ and $\mathbf{B} = 0.26\ m^4\ s^{-3}$ as the first two. They demonstrated that the 'mixed' case rapidly becomes plume like, with $\mathbf{l_m} = 4.5$ m, and that the mean dilution 60 m above the source is $\mu/Q = 68$, which is essentially that for a pure plume (and nearly three times that predicted for the jet).

1.2.2 The entrainment equations

The entrainment assumption will now be taken as the explicit starting point, i.e. it will be assumed that the inflow velocity at the 'edge' of the flow is some fraction α of the maximum mean upward velocity. Using the previous notation, this implies that

$$\frac{d\mu}{dz} = 2\pi b_w \alpha W_m \tag{1.10}$$

where $\mathbf{W_m}$ and $\mathbf{b_w}$ for Gaussian profiles are defined by (1.4). The 'entrainment constant' α clearly depends on the profile chosen, and it will be numerically different if equivalent 'top-hat' profiles are used. Its relation to the constants already given for jets and plumes will be discussed below. The larger spread of the time-averaged mass concentration given in (1.5) and (1.6) will also be taken explicitly into account. For both jets and plumes $\mathbf{b_\theta/b_w}$ has nearly the same constant value ($\mathbf{b_\theta/b_w} = \lambda$) equal to 1.2.

The equations of conservation of mass, momentum and buoyancy can be written; using Gaussian profiles and the Boussinesq approximation, in the following form (see Turner[9] and Fischer et. al.[10] for a more detailed discussion of the derivation and underlying assumptions):

$$\frac{d}{dz}(b_w^2 W_m) = 2\alpha b_w W_m$$
$$\frac{d}{dz}(\frac{1}{2} b_w^2 W_m^2) = \lambda^2 b_w^2 g\theta_m \qquad (1.11)$$
$$\frac{d}{dz}(\frac{\lambda^2 b_w^2 W_m g\theta_m}{1+\lambda^2}) = -b_w^2 W_m N^2(z)$$

With the more general application to stratified surroundings in mind, the third (buoyancy) equation includes, on the right, $N^2 = (-g/\rho_1)\,(d\rho_0/dz)$ the square of the local buoyancy frequency. The value of $g' = g\theta = g\,(\rho_0-\rho)/\rho_1$ is calculated using the local density difference between the plume ρ and its environment ρ_0 at height z, and ρ_1 is some standard density in the environment. Note again that the numerical coefficients in (1.11) depend on the form of the profiles, and the velocity and length scales used; they are different for 'top-hat' profiles. The equations can be solved once initial values of b_w, W_m and θ_m are specified, as they can be if **Q**, **M** and **B** are known.

For homogeneous surroundings ($N^2 = 0$), the similarity solutions are entirely equivalent to (1.11), and will in fact be particular solution of these equations. For the limiting cases of jets and plumes, Fischer et. al.[10] have used the experimentally determined parameters to show that (for Gaussian profiles)

$$\alpha_{jets} = 0.054, \quad \alpha_{plumes} = 0.083 \qquad (1.12)$$

This difference in entrainment rates for jets and plumes is consistent with the deductions made from (1.9b), which indicated that the dilution rate of a plume is higher than for a jet for the same local momentum flux. Deductions in (1.7b) and (1.9b) are based on experimental observations. There is no reason why C_p and C_j should be the same, and hence, the entrainment and the dilution rates are more of observations rather than being based on any theory.

Another point worth repeating is that the values of α given by (1.12) are only indirectly related to the angle of spread of the velocity profile in jets and plumes. For jets, (1.10) gives $\mathbf{db_w/dz = 2\alpha = 0.107}$, as already set out in (1.6). For plumes, the corresponding relation is $\mathbf{db_w/dz = (6/5)\ \alpha = 0.100}$, although this value is based on much less precise data. Thus the angles of spread are little different for jets and plumes, in spite of the fact that the 'entrainment rates' as defined above are substantially different. A constant angle of spread was suggested as a reasonable fit to all the experimental results on buoyant jets over the whole length of the flow, including the transition (List and Imberger[14]), though Chu et. al.[11] have reported anomalously small angles of spread in the transition region.

1.3 Other factors affecting entrainment

Experimental results of Bhat and Narasimha[3] have revealed a dramatic difference in the entrainment between jets and plumes subjected to off-source volumetric heating and their unheated counterparts. Experimental observations show that plumes entrain more rapidly than jets; the greater entrainment by the plume is typically attributed to the presence of buoyancy in the plume. In contrast, the addition of buoyancy *away from the source* by volumetric heating produces the opposite effect of reduced entrainment. Narasimha's group[3, 15, 16] has conducted a series of experiments and numerical simulations with jets and plumes subjected to volumetric heating to show that latent heat release during condensation above the cloud base is the key factor in reducing the rate of entrainment in clouds.

Apart from buoyancy, other factors that affect entrainment are flow acceleration or deceleration due to an applied pressure gradient along the flow or other body forces, and stratification of the ambient medium. Results from the reacting mixing layers indicate that entrainment is reduced by as much as 30% in a reacting mixing layer (flame) compared to the non-reacting mixing layer. This reduction is attributed to flow acceleration caused by dilation. Experiments of Choi et. al.[4] show that entrainment and mixing are high in jets subjected to an adverse pressure gradient, whereas the entrainment

is reduced or completely suppressed in a jet subjected to a favorable pressure gradient.[17] Entrainment is also inhibited in a jet when the injection velocity is increased in time[18], the effect arising from temporal variations and not spatial ones.

Based on the above experimental observations, Sreenivas K.R. and Ajay K. Prasad[6] have argued that the main factor that affects the entrainment process is the axial acceleration. By taking into account the axial acceleration factor in viewing all the entrainment data, the anomalous behavior of volumetrically heated jets and plumes is easily explained.

Apart from the above studies, there has been little fundamental research on mixing between streams with very different viscosities. Campbell and Turner[8] have studied a class of flows in which the extent of mixing between a turbulent fluid and its surroundings depends on the viscosity ratio between the two fluids. The context for the experiments reported by them is a geological one, the injection of a new pulse of magma into a magma chamber from below in the form of a 'fountain', but the results have a wider significance. For example, viscosity differences play an important role in engineering applications like the blending of differently viscous fluids in a process industry.

1.4 Campbell's work on viscosity effects: An overview[8]

When a turbulent 'fountain' of fluid of low viscosity ν_1 is injected upwards into a less dense fluid of higher viscosity (ν_2), the two fluids may mix thoroughly or not at all, depending on the relative magnitudes of an input Reynolds number $\mathbf{Re_1 = wd/\nu_1}$ and the viscosity ratio ν_2/ν_1 where **w** is the mean velocity and **d** is the diameter of the input. The criterion for mixing can be expressed alternatively as $\mathbf{wd/\nu_2 > k}$, a constant, in agreement with a more general theoretical argument which is also outlined in the paper.

In figure 1.3, a schematic of Campbell's experimental set-up is shown. A denser fluid (such as K_2CO_3 solution) is injected into a tank of another fluid (glycerol, water etc.) and

the amount of fluid that falls back after losing its entire upward momentum was measured to quantify entrainment. The total amount of fluid supplied to the fountain was recorded as the height $\mathbf{h_t}$ of the column of liquid added to the rectangular tank. The 'entrainment height' h was measured by subtracting $\mathbf{h_t}$ from the height $\mathbf{h_m}$ of the mixed or hybrid layer at the bottom of the tank, that is $\mathbf{h = h_m - h_t}$ (The hybrid layer will now have a gradient of viscosity, as well as density). The maximum entrainment in each series, equivalent to an entrainment height $\mathbf{h^*}$, was obtained at the minimum value of ν_2. The results for the different series of experiments are compared by normalizing **h** with $\mathbf{h^*}$ in each case and defining $\mathbf{H = h/h^*}$.

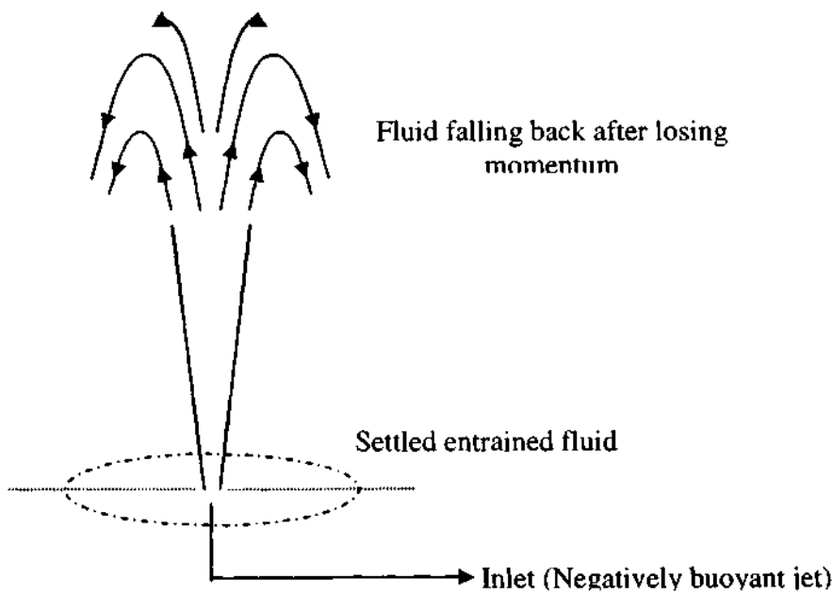

Figure 1.3: Campbell's experimental set-up

Figure 1.4 shows the main results of Campbell in a graphical form. Figure 1.4a represents the results of 'fountain' experiments carried out in a tank 400x196x297 mm deep, using a fixed nozzle 7.2 mm diameter and three inflow rates, corresponding to the different symbols. The normalized entrainment **H** ($=\mathbf{h / h^*}$, as explained above) is plotted against the viscosity ν_2 of the host fluid in centistokes, on a logarithmic scale. The arrows mark the viscosities at which the entrainment is predicted (using a simple theoretical model) to

fall to half its maximum value in the experiments with **wd** = 18 cm^2 s^{-1} and **wd** = 3.9 cm^2 s^{-1}. The displacement of these arrows from the corresponding experimental curves is a measure of the direct effect of ν_1 in reducing entrainment.

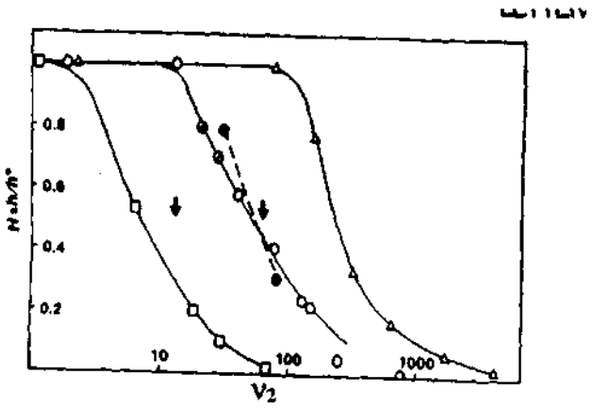

Figure 1.4a): Variation of entrainment with ambient viscosity at different inlet flow rates

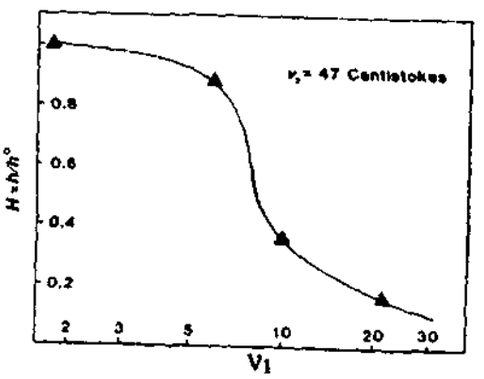

Figure 1.4b): Variation of entrainment with inlet viscosity

Figure 1.4b represents a plot of the amount of entrainment **H** against ν_1 (in centistokes) on a logarithmic scale, measured in experiments with constant ν_2 (=47 centistokes) and wd = 18 cm^2 s^{-1}. The measured entrainment heights have been normalized to the amount of entrainment ($\mathbf{h^0}$) expected from the previous experiments with **wd** = 18 cm^2 s^{-1}, as read from figure 1.4a.

The results are summarized as follows:

1. For any value of **wd**, there is a critical value of $\nu_2 (= \nu_2^c)$ below which changes in the viscosity of the host fluid have no influence on mixing.
2. Once $\nu_2 > \nu_2^c$, the viscosity of the host fluid has a controlling influence on entrainment, which then falls sharply and becomes very small at values of $\nu_2 > 10\nu_2^c$.
3. The higher the value of **wd**, the higher is the value of ν_2 at which the viscosity of the host fluid first influences entrainment.

Some of the possible sources of errors in the above experiment are:

1. Since the fluid after losing its momentum falls back through the ambient fluid before settling down, it will possibly entrain some more fluid while falling back. This additional entrainment is not accounted for in the experiments.
2. The fluid that falls back, seriously affects the dynamics of the actual jet.

Considering the above points, we decided to conduct experiments in a set-up with a standard configuration (and hence avoid the above stated problems) and conduct a more detailed study of the same problem. In this work, we study the entrainment happening in a jet/plume/buoyant jet and concentrate on the mechanisms that control the process. The study is carried out via experiments and 2-D simulations using vortex methods. Qualitative and quantitative conclusions are made from the current study.

Chapter 2

Experiments: Details and Specifications

All the experiments were conducted in a glass tank of dimensions 30x30x45 cm^3. Pipettes with an internal diameter of 1.3-1.4 mm at the exit were used to discharge the jet vertically down in the tank. The tank was filled with aqueous solutions with different viscosities and a specific density. Brine solution (of density greater than that of the fluid in the main glass tank) was discharged through the pipette. Densities of fluids were altered by the addition of suitable amounts of salt. Viscosities of the ambient fluid were altered by the addition of suitable amounts of Sodium carboxymethyl cellulose (Na-CMC). To ensure that CMC dissolves entirely in water, viscous solutions containing CMC were prepared at least a day before they were used in the experiments. The discharge velocity was maintained constant by using a constant head arrangement discharging across a constant resistance, as suggested by Debopam Das et. al.[20] The arrangement is explained below.

2.1 Constant pressure-head flow set-up

Figure 2.1 represents the schematic of the constant pressure-head flow set-up. The discharge tube (pipette) was connected to a five litre aspirator bottle through two valves, with one of them having fine control. Water level was maintained in a capillary tube attached to the top of the aspirator bottle. To get constant flow rate, this level was kept constant through a constant flow into the capillary from another constant head constant resistance arrangement. This consists of a two-litre aspirator bottle with a fine control valve discharging into atmospheric pressure. Here, level in the two-litre aspirator bottle provides the constant head, and valve and tubing the resistance. Here, the fine control valve from the two-litre aspirator bottle discharges into atmospheric pressure, either into the capillary on top of the five-litre aspirator bottle or a burette outside for measuring the flow rate. Flow rate was measured by measuring the time taken to collect a specific volume of the fluid. The fine control valve from the two-litre aspirator bottle is adjusted at the start of every experiment so that the level of the fluid in the capillary does not change during the experiment.

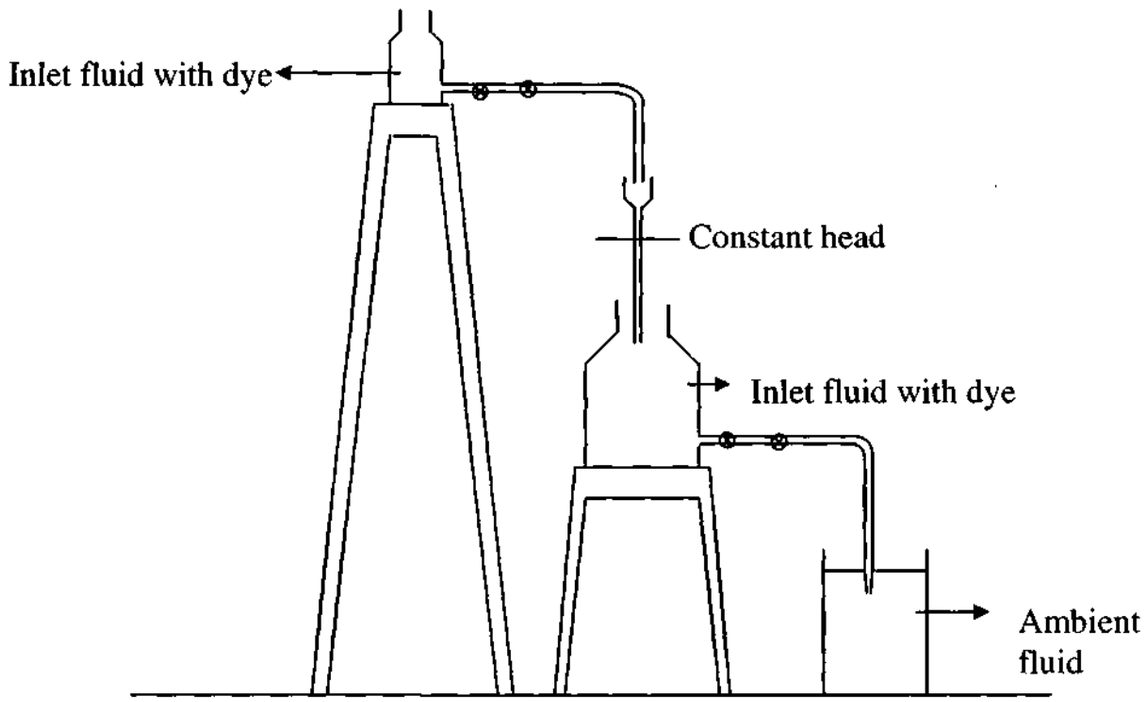

⊗ : Flow control valve

Figure 2.1: Constant pressure-head flow set-up

2.2 Main Tank

As specified earlier, the main tank was of dimensions 30x30x45 cm^3. The inlet fluid is denser than the ambient fluid and always possesses downward momentum. The inlet fluid, along with the entrained ambient fluid, hits the bottom of the tank with a finite momentum and bounces back. This leads to mixing of the entrained fluid with the ambient fluid. To avoid this problem, a high-density layer (fluid of density greater than that of both the inlet and the ambient fluids) was placed at the bottom of the tank. Now, the entrained fluid possessing downward momentum hits the high density layer at the bottom, loses all of its kinetic energy and settles nicely above this bottommost layer. The entrained fluid being heavier than the ambient fluid stays below the ambient fluid. As most of the kinetic energy in the jet is absorbed while bouncing off from the bottommost fluid layer, mixing of the entrained-jet-fluid with the ambient fluid is suppressed. A

schematic of the main glass tank is shown in figure 2.2. Densities of different fluids were measured by measuring the mass of a specific volume of the fluid.

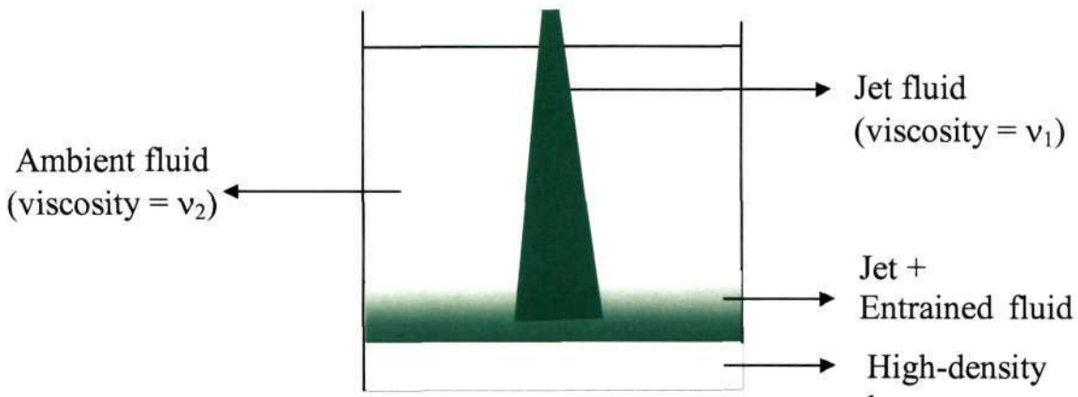

Figure 2.2: Main tank

2.3 Viscosity measurement

Viscosities of fluids were experimentally determined using the Stokes law for a sphere falling inside a fluid at low enough Reynolds numbers. For a spherical object of radius r, at low speeds the surrounding fluid flow is laminar. The resistance force exerted by a viscous fluid on a spherical object of radius 'r' moving through it with constant velocity is given by

$$\mathbf{F}_{\mathbf{viscous}} = (6\pi) \text{ x } (\mu) \text{ x } (r) \text{ x } (v)$$

where μ is the dynamic viscosity of the fluid and v the terminal velocity attained by the spherical object. This is valid only for Reynolds number less than 80, where the flow is substantially laminar.

For the spherical object in force equilibrium, the viscous force mentioned above and the buoyancy force exerted by the fluid balance its weight.

$$V_{ball}(\rho_{ball}-\rho_{fluid})g = \mathbf{F}_{\mathbf{viscous}}$$

where $\mathbf{V}_{\mathbf{ball}}$ is the volume of the spherical ball, $\rho_{\mathbf{ball}}$ its density, $\rho_{\mathbf{fluid}}$ the fluid density, **g** the acceleration due to gravity and $\mathbf{F}_{\mathbf{viscous}}$ the viscous drag force.

Spherical balls (of diameter ~ 5.9 mm) of different densities were dropped into the fluid whose viscosity is to be measured. The density difference between the ball and the fluid was made small enough to ensure low speeds and hence low Reynolds numbers. The balls were allowed to fall through one metre column of the fluid. The time taken to travel the last 50 cm was noted down and in turn the terminal speed of the ball was estimated. The initial 50 cm of the fluid is large enough to ensure that the ball attains terminal velocity.

2.4 Flow visualization

The plane containing the centerline of the jet was illuminated using a 532 nm Nd-Yag laser light sheet. The laser beam was converted into a planar light sheet using a plano-concave cylindrical lens. Reflecting mirrors were used to deflect the laser beam as per requirement. Figure 2.3 represents a schematic of the laser light sheet illumination of the main glass tank.

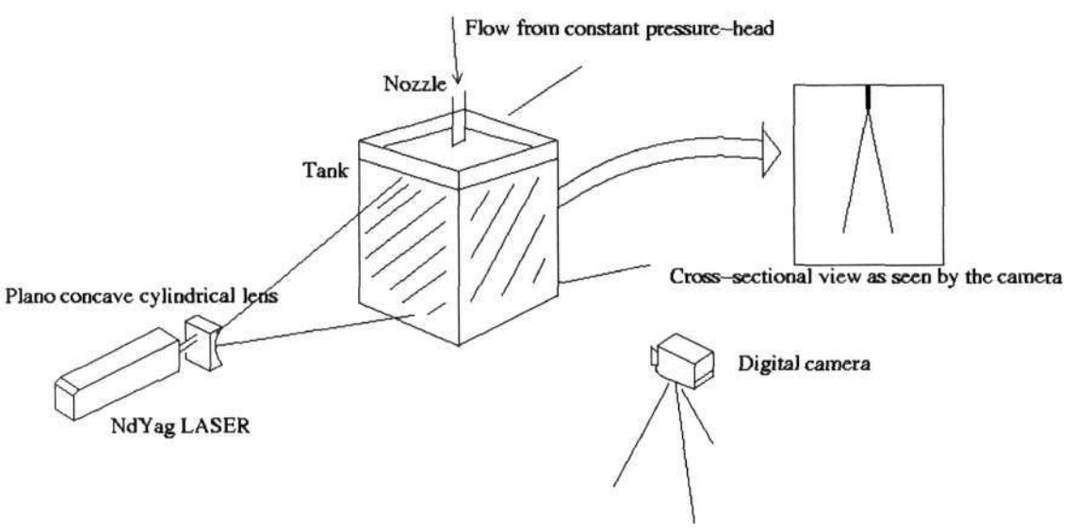

Figure 2.3: Schematic of the flow visualization arrangement

Fluorescein dye was added to the inlet fluid for flow visualization purposes. A Nikon Coolpix 990 camera was placed such that the plane of the jet that was illuminated was viewed in a normal direction.

Both instantaneous and time-averaged images were taken in all the experiments. Instantaneous images were taken by keeping the shutter of the camera open for a while and a single pulse of the laser given during this time. The duration of the pulse being very small (5-7 nanoseconds), the image taken by this procedure will represent the flow field at a certain instance. The flow structure becomes evident in these instantaneous images. Time-averaged images are taken by keeping the shutter of the camera open for quite some time (~ 8 seconds) and around 10-12 laser pulses given during this. Images of the jet at 10-12 different instances superimposed on the same frame represent a time-averaged picture of the flow. Jet-widths (Scalar spread of the inlet fluid) and the laminar length (the distance from the nozzle-exit till where the jet remains laminar) are estimated from the time-averaged images. Subtracting out the minimum intensity levels that are existent throughout the image filters the raw images obtained. The jet-width at any axial location is defined as the radial location (at that axial position) at which the intensity of green light becomes $(1/e)^{th}$ of that at the centerline.

2.4.1 Streak photography

The ambient fluid was seeded with fine aluminium powder. These particles were passive scalars following the fluid flow faithfully. Images were taken by keeping the camera shutter open for around 10-15 seconds with the laser illuminating the flow at 40 Hz during this period. The images taken show clearly the streaks formed by the particles in the ambient fluid. These images help in getting a qualitative picture of the flow-field outside the scalar spread of the jet (indicated by the extent to which the green colour of the inlet fluid has spread).

2.5 Entrainment quantification

We have also performed experiments where quantitative data on how much entrainment happens were measured. As explained in Sec 2.2, the inlet fluid along with the entrained fluid (green-coloured because of the presence of fluorescein dye) settles down as a distinct layer in between the bottommost layer and the ambient fluid. The height of the settled- down green layer in a specific duration of time represents the amount of entrainment that has happened during that time (the green layer comprises both the inlet fluid that has been pushed in and the entrained ambient fluid). The duration is made short enough so that the settling down fluid does not affect the actual jet drastically. Also, at the same time, the duration is made long enough so that there is a clear discernable height of entrained green fluid that settles down.

2.6 Results

The results from the experiments are presented in this section. Only the relevant parameters in the experiments and a brief explanation of the figures are given here. A detailed discussion is given in Chapter 4. All the results shown in this section correspond to the following values for the densities of the inlet and the ambient fluid.

$$\rho_{inlet} = 1099 \text{ kg / m}^3 \qquad \rho_{ambient} = 990 \text{ kg / m}^3$$

The exit diameter of the inlet nozzle was **1.4 mm**. The dynamic viscosity of the inlet fluid was always **0.001 Ns/m^2**.

The Morton length-scales (defined in **1.2.1**) corresponding to different inlet Reynolds numbers, for the specific density difference at which the experiments were conducted, are listed in table 2.1. The inlet Reynolds number was calculated based on the inlet velocity, the inlet diameter and the kinematic viscosity of the inlet fluid.

Even though the buoyant jet becomes plume-like at axial locations that are as high as $60\mathbf{d}_{inlet}$for high inlet Reynolds numbers, the Morton length-scale corresponding to most of our experiments (whose inlet Reynolds numbers were within 2000) is within 4.5 cm

Inlet Reynolds Number (**Re**)	Morton length-scale $\mathbf{l_m}$ (cm)	$\mathbf{l_m/d_{inlet}}$
1 - 100	0.0022 – 0.22	0.0157 – 1.57
100 - 500	0.22 – 1.1	1.57 – 7.86
500 - 1000	1.1 – 2.2	7.86 – 15.71
1000 - 1500	2.2 – 3.3	15.71 – 23.57
1500 - 2000	3.3 – 4.4	23.57 – 31.43
2000 - 2500	4.4 – 5.5	31.43 – 39.29
2500 - 3000	5.5 – 6.6	39.29 – 47.14
3000 - 3500	6.6 – 7.7	47.14 - 55
3500 - 4000	7.7 – 8.8	55 – 62.9

Table 2.1

from the inlet (corresponding to an axial location ~ $30\mathbf{d_{inlet}}$). This means that we are effectively studying a buoyant jet that becomes plume-like very quickly. The Morton length scales of all the experiments are presented alongside the figures. Data from regions that are well within the Morton length-scale are also presented.

The following are the notations used for various parameters in all the figures.

$\mathbf{Re_{inlet}}$ – Inlet Reynolds number

ν_1 – Kinematic viscosity of the inlet fluid

ν_2 – Kinematic viscosity of the ambient fluid

2.6.1 Flow visualization

Figures 2.4 a) and b) depict instantaneous pictures of a fully turbulent buoyant jet. Notable features here are the presence of coherent structures and the rapid entrainment that takes place. Correlation between the coherent structures and the entrainment will be discussed later. The dye used is fluorescein dye and the illumination is by 532 nm laser light sheet.

a) A zoomed-out view

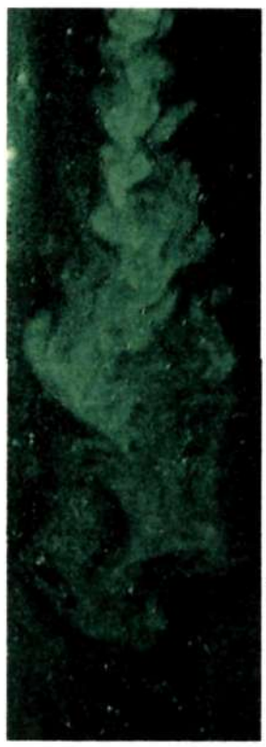

b) A zoomed-in view

Figure 2.4: Fully turbulent buoyant jet and associated entrainment
$Re_{inlet} = 700$, $\nu_2 = \nu_1$

Figure 2.5 gives a qualitative flavor of the effects of the ambient viscosity on entrainment. The dye used in these experiments is potassium permanganate. We observe appreciable entrainment in figure 2.5 a), which corresponds to a case where the viscosity of the ambient fluid is equal to that of the viscosity of the inlet fluid. At the same Reynolds number, we can observe that the entrainment is completely suppressed when the viscosity of the ambient fluid is much higher in comparison with that of the inlet fluid. Both are time-averaged images. The exact value of the ambient viscosity in figure 2.5 b) is not known. The bottommost parts of each of the images indicate the colored entrained fluid that has settled above the bottommost high-density layer.

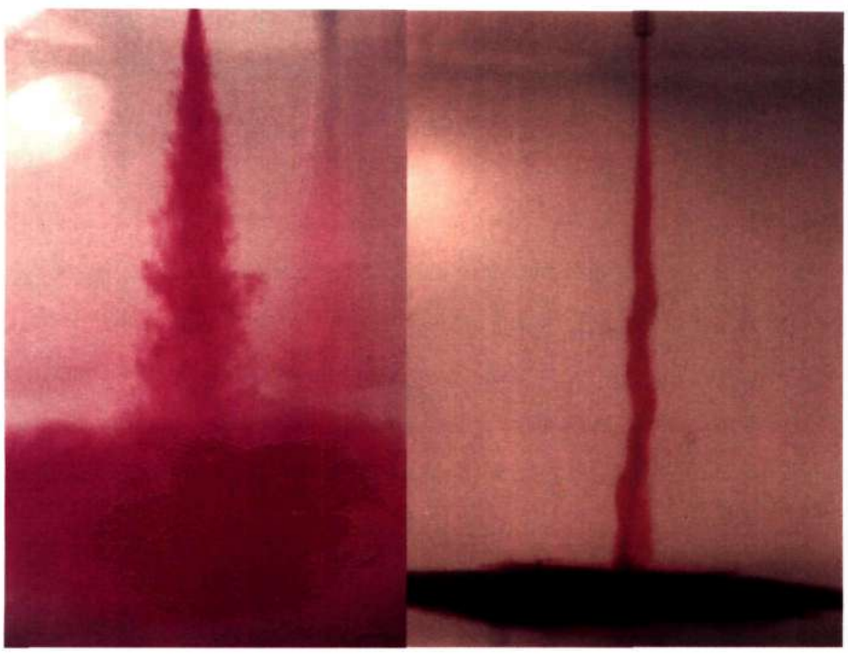

a) Re_{inlet} = 1700 **b) Re_{inlet} = 1700**

$\nu_2 = \nu_1$ **Ambient fluid – more viscous than the inlet fluid**

Figure 2.5: Suppression of entrainment by ambient viscosity

Figure 2.6 represents a set of time-averaged images of the flow for similar inlet Reynolds numbers (~100) but for increasing ambient to inlet viscosity ratios. The extent to which the green colour has spread is an indication of the scalar spread rate (scalar referring to the inlet fluid particles), which in turn means how much entrainment and hence mixing is happening. Since the Reynolds number is very low in all the cases shown in this figure, we are effectively looking into the behavior of a plume as the corresponding Morton length scales (as shown in Table 2.1) are very small. Appreciable noise in all these images can be attributed to the murkiness of the ambient fluid, which is unavoidable. We observe that the ambient viscosity plays an important role in suppressing the entrainment (scalar spread rate). We also observe from the figure that, the effects of the ambient viscosity on the entrainment become important only after a specific viscosity ratio is reached. We observe not much difference in the scalar spread rate between the cases where the viscosity ratio is one and eleven respectively. We observe an appreciable suppression of entrainment in the case where the viscosity ratio is 15. This

specific viscosity ratio, above which the ambient viscosity starts playing a prominent role in the entrainment process, will be different for different inlet Reynolds numbers. This result is supportive of the qualitative conclusions that are drawn by Campbell and Turner.[8]

Figure 2.7 shows the instantaneous images of the entire cases shown in figure 2.6. It is interesting to observe that the coherent structures that are very prevalent in the case that corresponds to a viscosity ratio of unity are completely absent in the final case in which the viscosity ratio is 47. It seems that, the ambient viscosity plays a key role in suppressing structures at the interface that are of shorter wavelengths. Structures of longer wavelengths are still present even in the high viscosity ratio case. The entrainment (and hence mixing) that is happening seems to be strongly correlated with the presence of coherent structures at the interface between the inlet jet fluid and the ambient fluid. This correlation is consistent with the results presented by Sreenivas[21].

Time-averaged figures (similar to the ones shown in figure 2.6) were analyzed to estimate the scalar spread width (in this case it is the same as the extent to which the green color of the inlet fluid has spread) for different cases. Variation of the scalar spread width with the axial location, inlet Reynolds number (for the same viscosity ratio) and viscosity ratio (for the same inlet Reynolds number) are plotted later in this chapter.

Figures 2.8 and 2.9 represent a set of time-averaged and instantaneous images respectively, taken for similar inlet Reynolds numbers (~830) but for increasing viscosity ratios. Qualitatively, the results are similar to what are shown in the figures 2.6 and 2.7, the difference being in the magnitude of the inlet Reynolds number. It can be concluded from these figures that the viscosity ratio beyond which it starts playing a prominent role in affecting the entrainment, is higher for higher inlet Reynolds numbers. The earlier comments made on coherent structures and long-wavelength structures are validated again in these two figures. The Morton length scales here are again small enough so that the flow can be considered plume-like beyond an axial location that is fifteen times the inlet diameter.

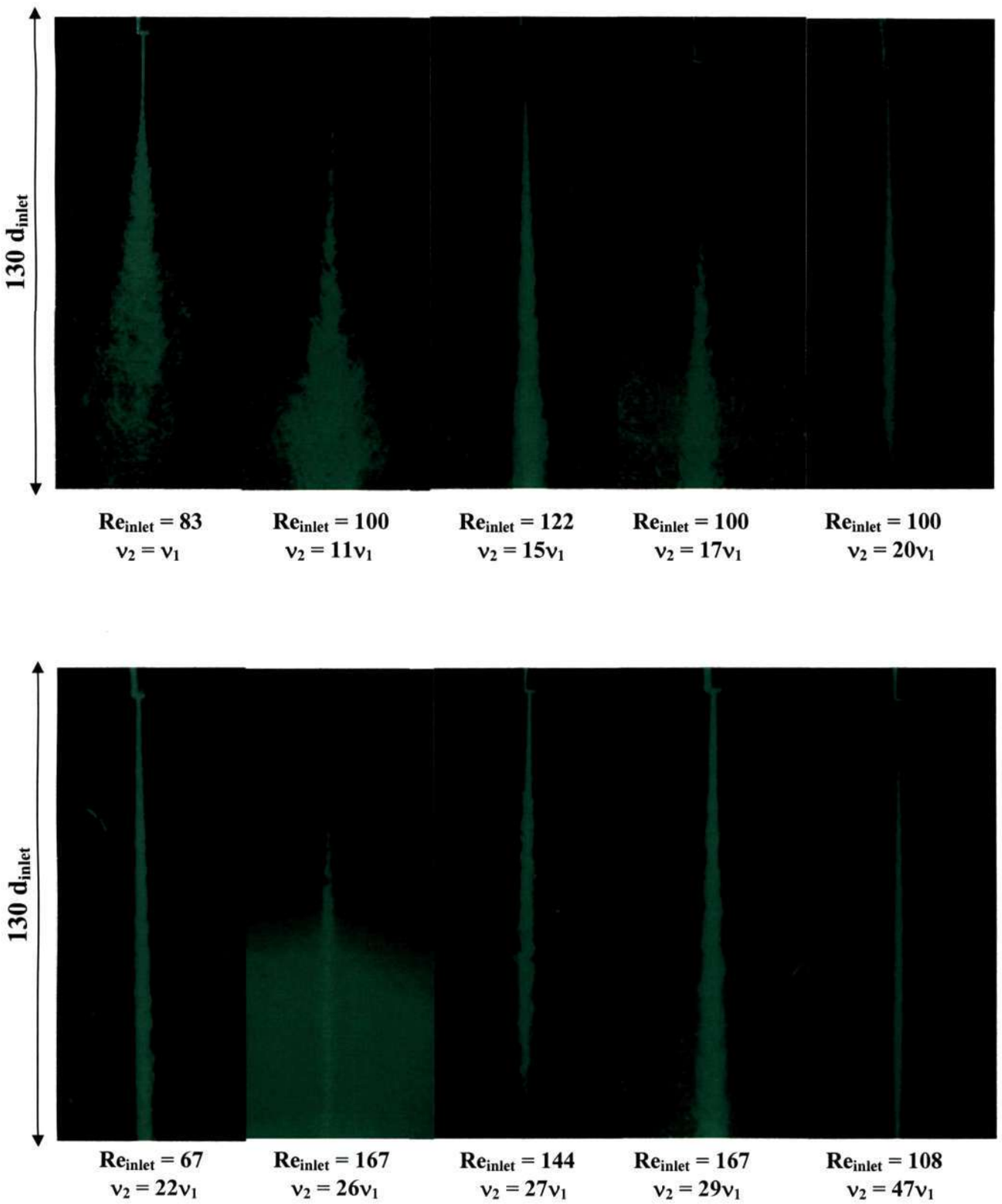

Figure 2.6: Entrainment at similar Re_{inlet} and increasing viscosity ratios (time-averaged)

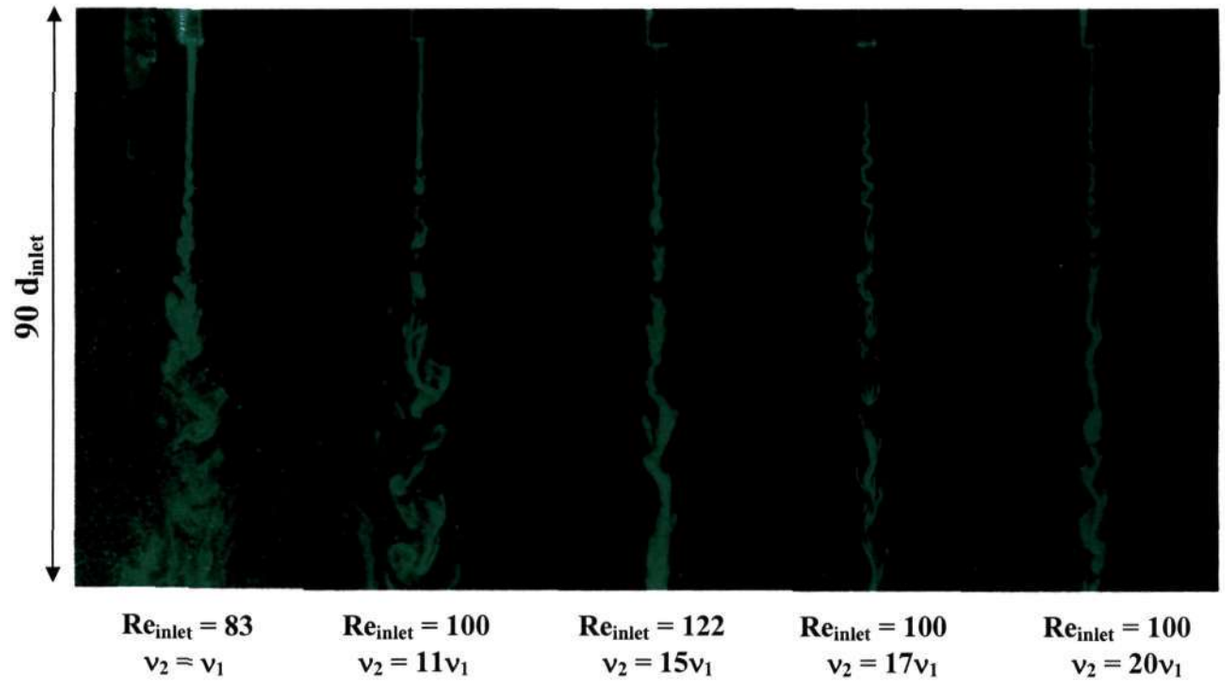

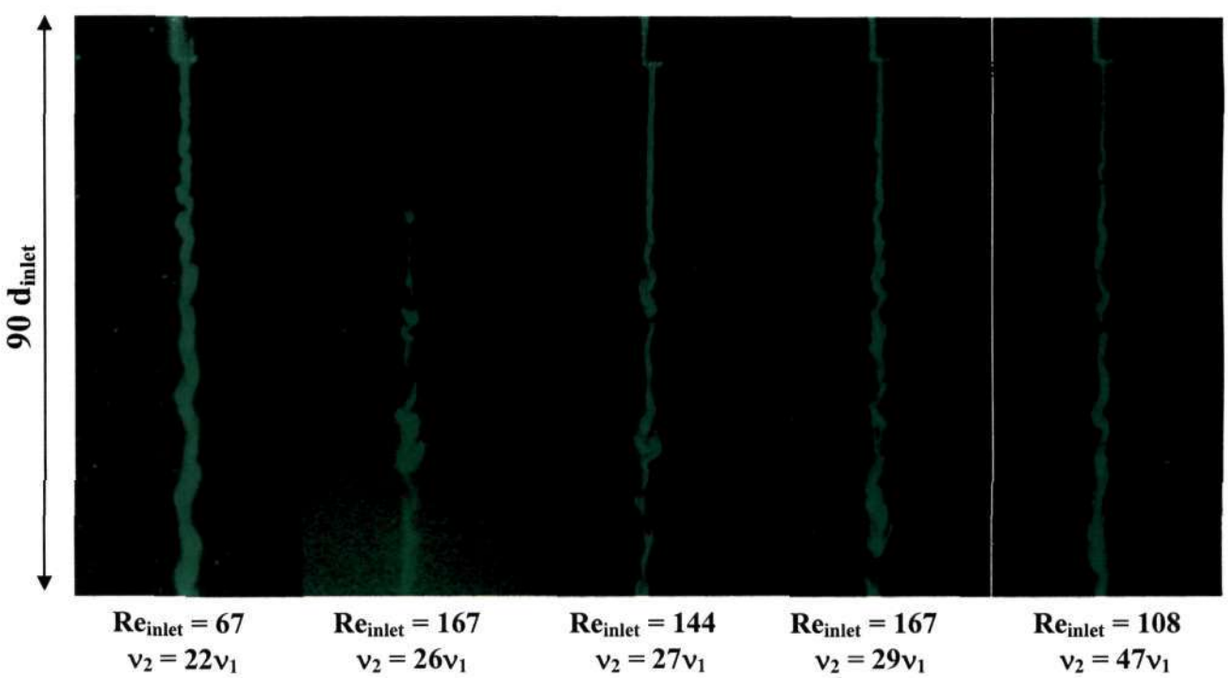

Figure 2.7: Entrainment at similar Re_{inlet} and increasing viscosity ratios (instantaneous)

Figure 2.8: Entrainment at similar Re_{inlet} and increasing viscosity ratios (time-averaged)

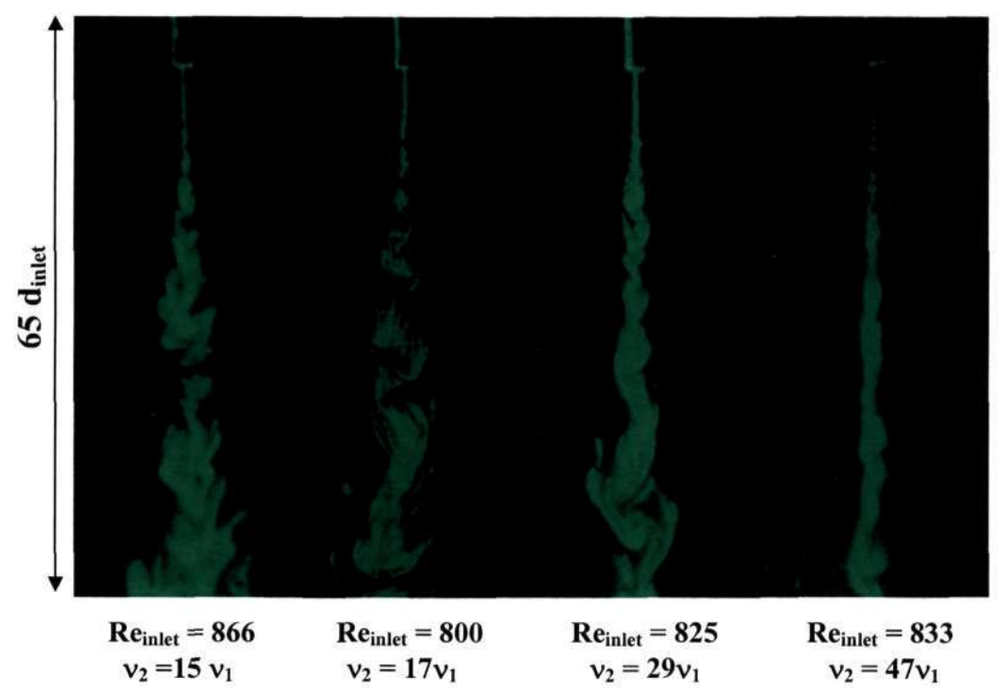

Figure 2.9: Entrainment at similar Re_{inlet} and increasing viscosity ratios (instantaneous)

Experiments were performed at higher inlet Reynolds numbers also, but the corresponding images are not presented here, as the qualitative conclusions remain the same as above. The data from these experiments were used for the plots shown later.

In figures 2.10 and 2.11, we show the variation of the scalar spread rate with increasing inlet Reynolds numbers, at the same viscosity ratio of 15. Figures 2.10 and 2.11 represent time-averaged and instantaneous flow patterns respectively. We observe that the effects of the ambient viscosity are more prominent at lower inlet Reynolds numbers and the suppression of entrainment becomes negligible at higher Reynolds numbers. The instantaneous images clearly show the presence of the longer-wavelength waves even at low inlet Reynolds numbers. The emergence of the coherent structures as the inlet Reynolds number increases seems to be well correlated with the increase in the scalar spread rate. There exists an inlet Reynolds number (specific to the viscosity ratio) beyond which the effects of the ambient viscosity on the entrainment are hardly present. This means that, beyond the particular inlet Reynolds number, we will observe hardly any increase in the scalar spread rate with increasing inlet Reynolds number, working at the same viscosity ratio. This result agrees well with the qualitative picture that Campbell and Turner have presented in [8].

Figures 2.12 and 2.13 present results similar to those in the figures 2.10 and 2.11, the only difference being in the viscosity ratio (ν_2/ν_1 = **27 in these figures**). The same analysis has been extended to a much higher viscosity ratio (ν_2/ν_1 = **47**) and the results are presented in figures 2.14 and 2.15. The variation in the scalar spread rate that we observe in these figures agrees well with the conclusions made from figures 2.10 and 2.11. Also, the inlet Reynolds number beyond which there is no change in the entrainment even with an increase in the inlet Reynolds number seems to increase with an increase in the viscosity ratio.

Interesting to note are a few bright spots in the images corresponding to high inlet Reynolds numbers at a fairly high viscosity ratio. For example, we observe this in both

Figure 2.10: Entrainment at varying Re_{inlet} (ν_2/ν_1 = 15) (time-averaged)

Figure 2.11: Entrainment at varying Re_{inlet} (ν_2/ν_1 = 15) (instantaneous)

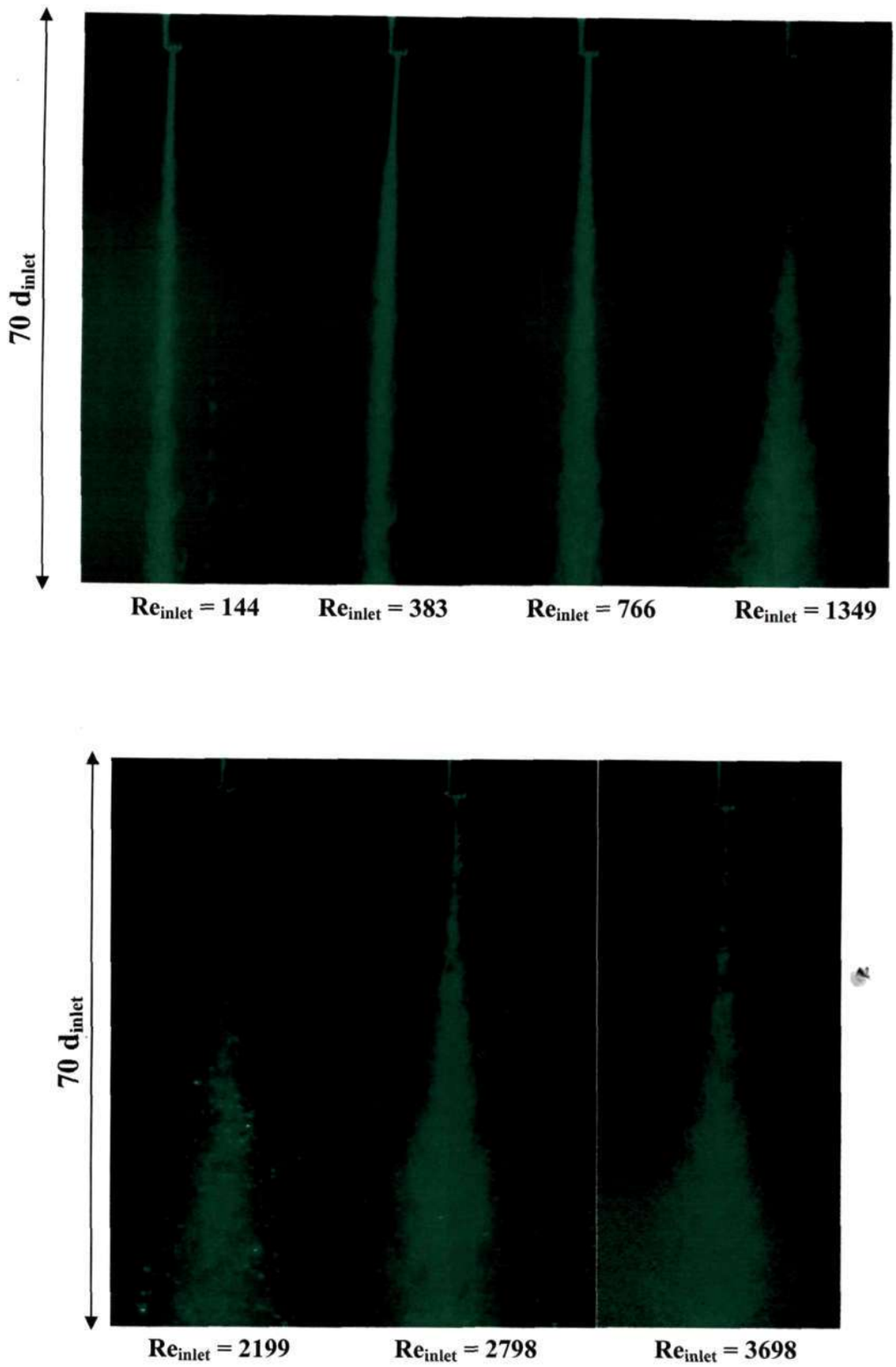

Figure 2.12: Entrainment at varying Re_{inlet} ($\nu_2/\nu_1 = 27$) (time-averaged)

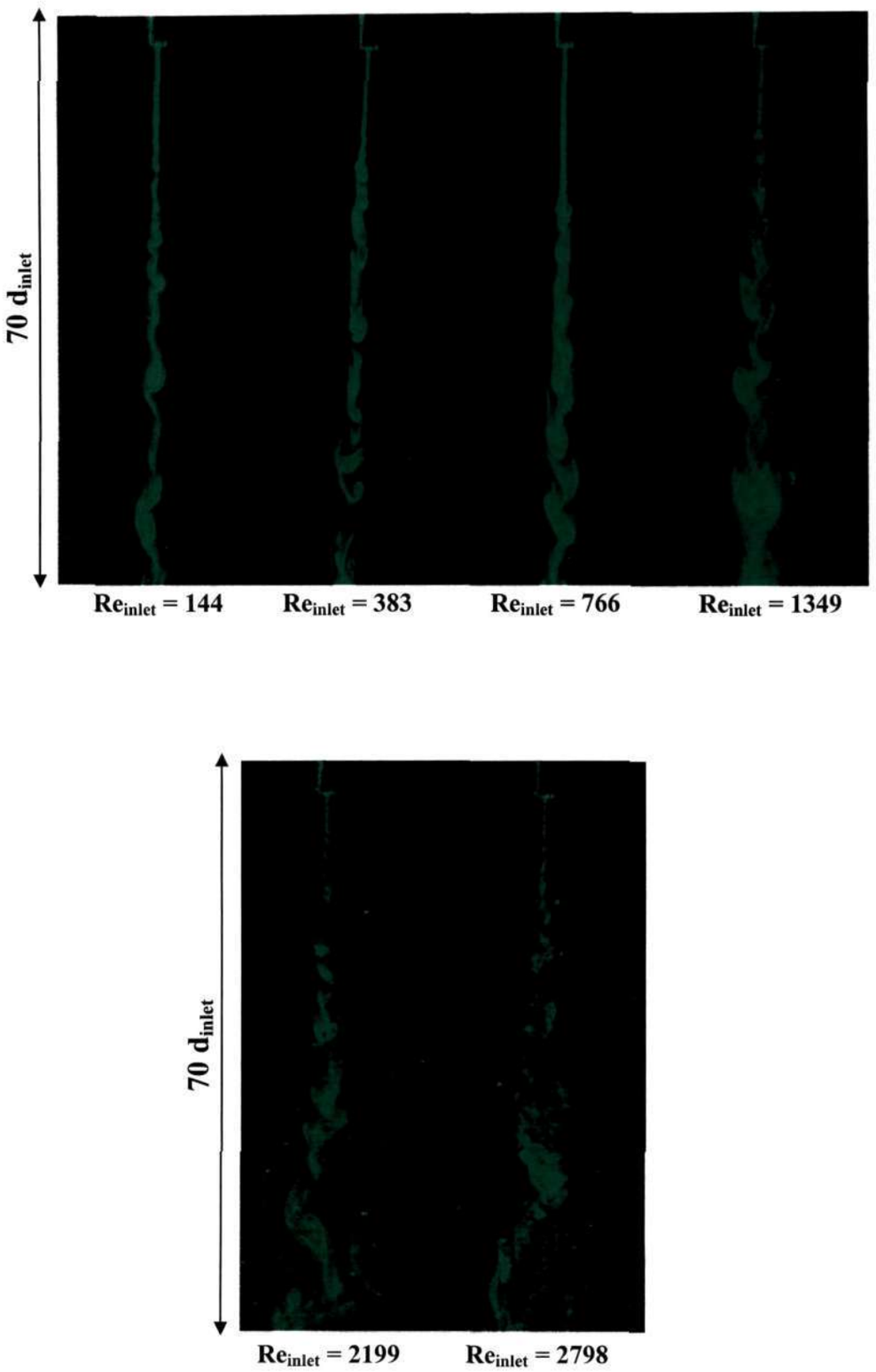

Figure 2.13: Entrainment at varying Re_{inlet} ($\nu_2/\nu_1 \approx 27$) (instantaneous)

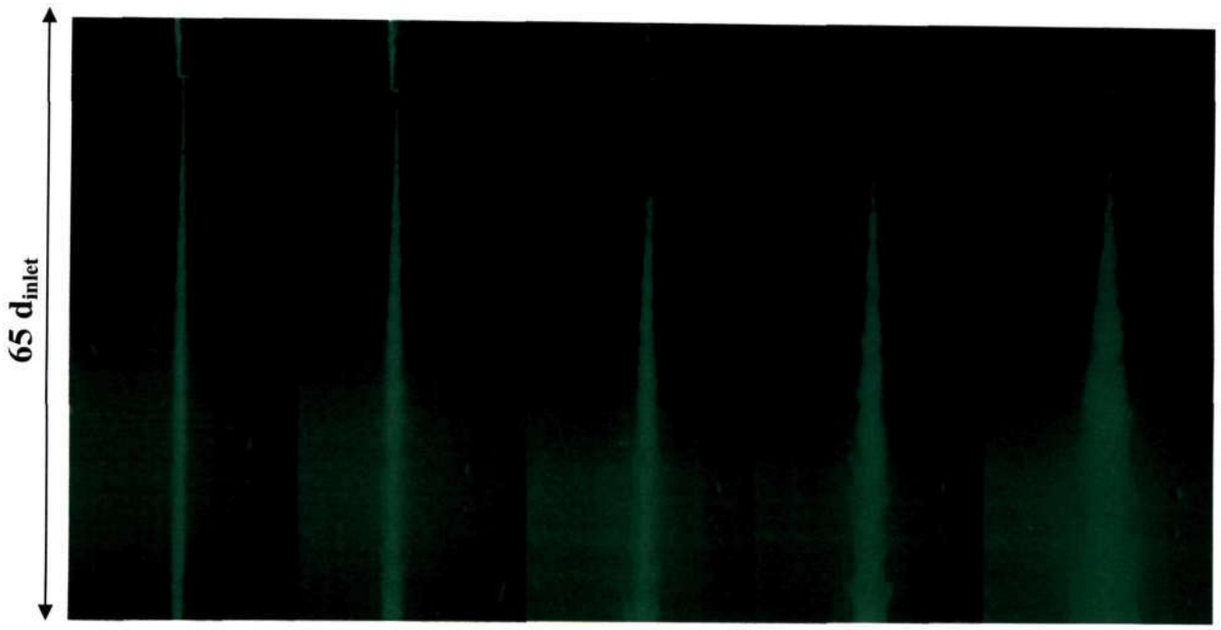

Re_{inlet} = 108 Re_{inlet} = 200 Re_{inlet} = 425 Re_{inlet} = 833 Re_{inlet} = 1999

Figure 2.14: Entrainment at different Re_{inlet} (ν_2/ν_1 = 47) (time-averaged)

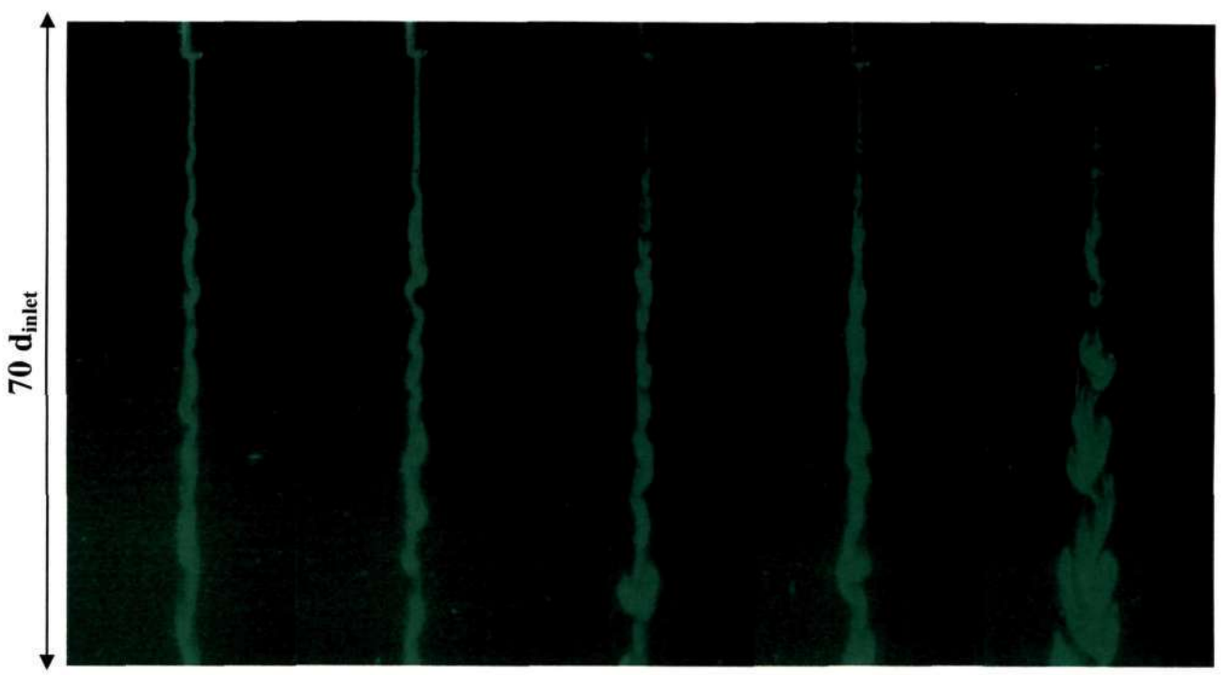

Re_{inlet} = 108 Re_{inlet} = 200 Re_{inlet} = 425 Re_{inlet} = 833 Re_{inlet} = 1999

Figure 2.15: Entrainment at different Re_{inlet} (ν_2/ν_1 = 47) (instantaneous)

the instantaneous and the time-averaged images of the case corresponding to a viscosity ratio of 27 and inlet Reynolds numbers of 2199 and 2798 (figures 2.12 and 2.13). These were bubbles that were continuously rising up in the tank, after being formed somewhere in the middle of the tank. Even though we do not have a clear reason for why they appeared, it could be interesting to look into. Their origin could also have been because of some air gap that was formed inside the tank before the experiments started. This has anyway been brought to notice because the bubbles were observed in more than one experiment.

2.6.1.1 Scalar spread widths: Variation with Re_{inlet} and ν_2/ν_1

As was explained earlier in this chapter, the extents to which the inlet fluid spreads (at different axial locations) in all the experiments were evaluated using the distribution of the light intensity in the green wavelength range. The scalar width gets specified by the radial location where the intensity of green light drops to $(1/e)^{th}$ of the centerline green intensity. Since there was appreciable noise in many of the images, accurate estimate of the scalar spreads could not me made. The following graphs are used primarily to explain

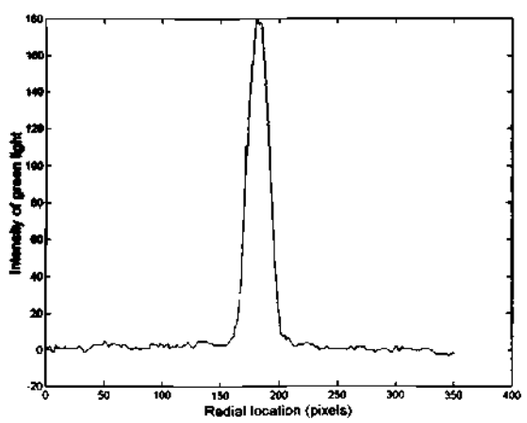

Figure 2.16: Intensity variation with less noise

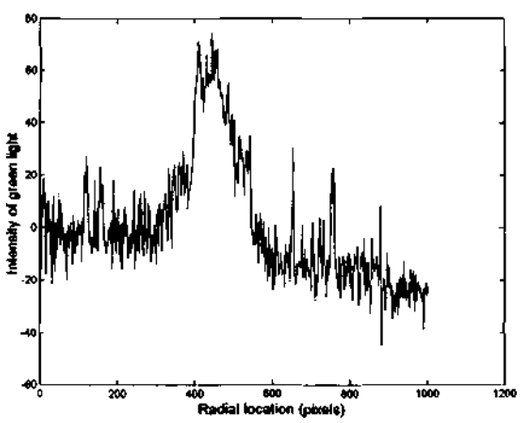

Figure 2.17: Intensity variation with appreciable noise

some of the qualitative aspects of the problem. Figure 2.16 shows the typical intensity plot when the noise is very low. In figure 2.17, we show a plot that has an appreciable amount of noise and this makes the estimate of the scalar spread very difficult. The two main factors that result in the noise are murkiness of the ambient fluid and non-uniformity of the laser illumination.

In figures 2.18, 2.19 and 2.20, the variation of the scalar width with the axial location for different cases is shown. The trend in the variation depends largely on the inlet Reynolds number and the viscosity ratio. The jet is conical (with a constant angle of spread) only when it is fully turbulent (and hence self-similar). In all the cases, we observe that the rate of change of the scalar width with the axial distance from the inlet is very low in the region where the jet is laminar. This can be attributed to the absence of coherent structures in this region, and will be discussed more in detail in chapter 4.

The variation of the scalar width beyond the laminar region strongly depends on whether the jet becomes fully turbulent or not. In the cases where ambient viscosity is playing an important role in suppressing the entrainment, the scalar width tends to remain constant beyond some axial distance. Also, we have plotted the variation of the scalar width at a particular axial location (and a particular viscosity ratio), against the inlet Reynolds number and observe that variation tends to be fairly linear till a particular value of the inlet Reynolds number, beyond which the variation is slower. This particular value of the inlet Reynolds number, beyond which the variation becomes slower, depends strongly on the viscosity ratio. These are plotted in figures 2.21, 2.22 and 2.23.

Another interesting result was observed when a passive scalar (food color, in this case) was released far away from the jet. As we observe in figure 2.24, even though the inlet fluid is restricted to a very small width, the momentum has diffused over a much wider region. The inlet Reynolds number and the viscosity ratio for this experiment are specified alongside the figure. The blue outer dye streak indicates the spread of momentum into the ambient, whereas the jet fluid is confined to a smaller region. Based

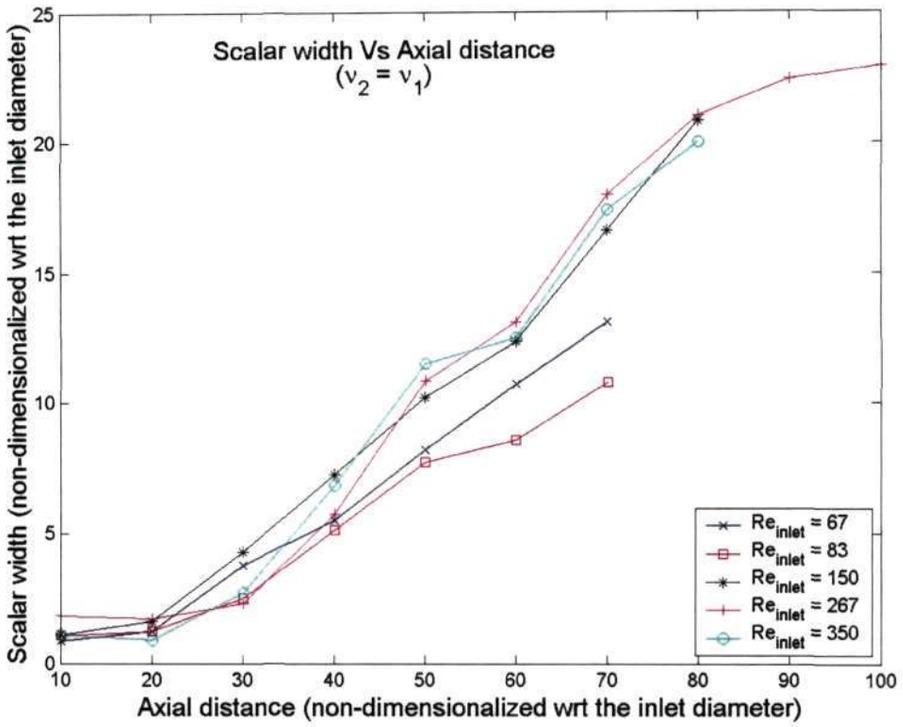

Figure 2.18: Scalar width Vs Axial distance

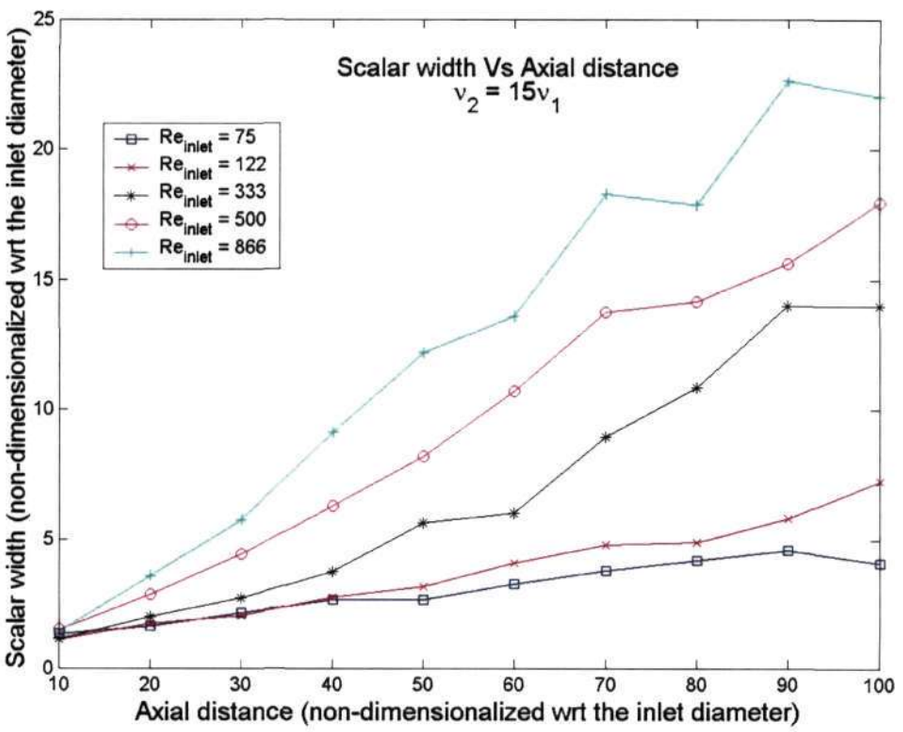

Figure 2.19: Scalar width Vs Axial distance

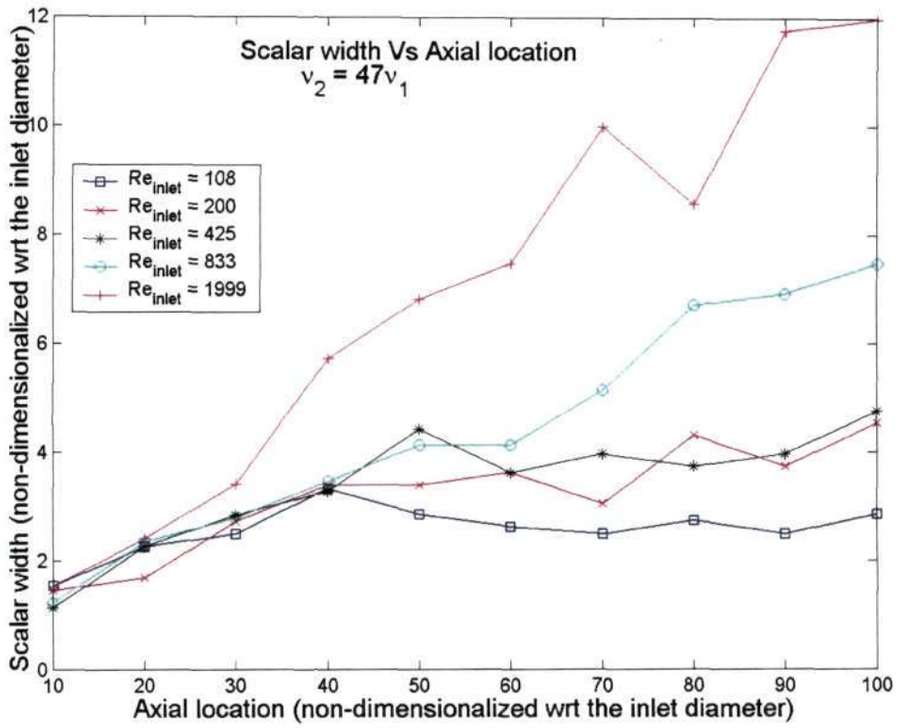

Figure 2.20: Scalar width Vs Axial distance

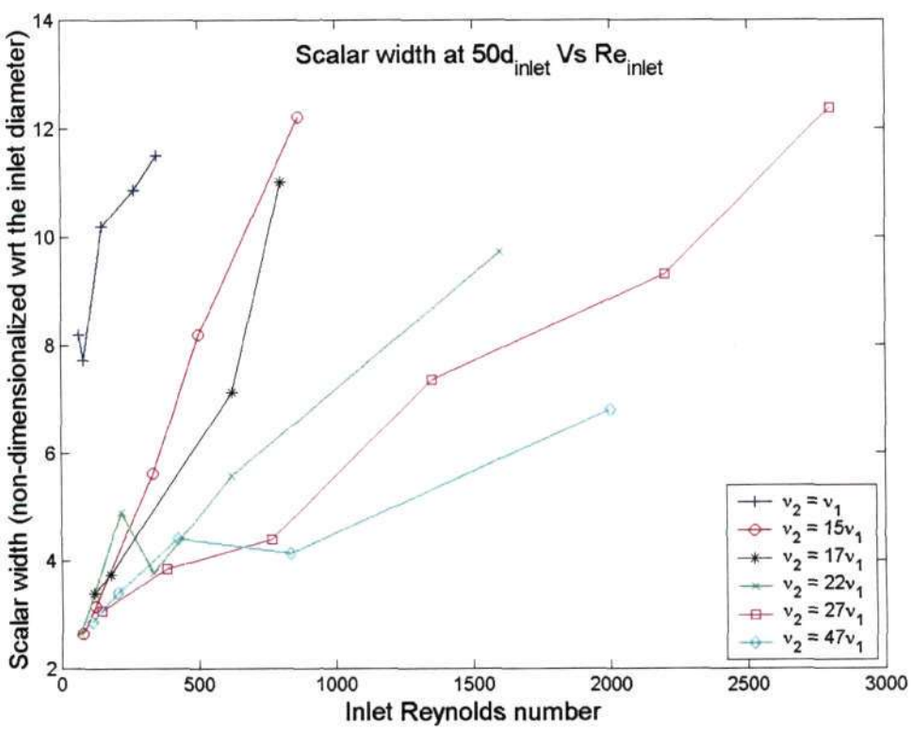

Figure 2.21: Scalar width (at $50d_{inlet}$) Vs Inlet Reynolds number

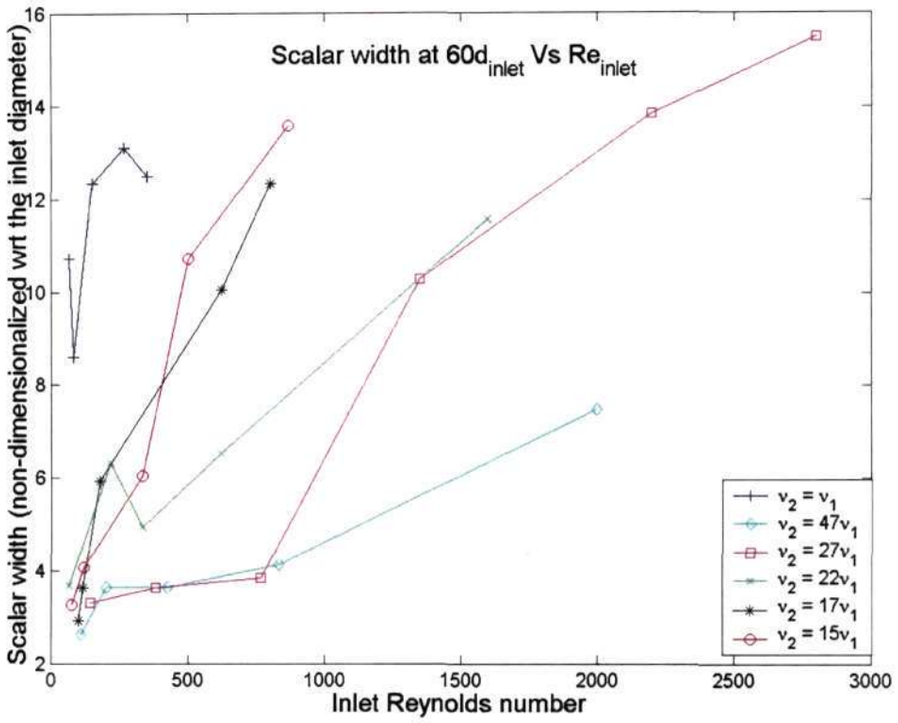

Figure 2.22: Scalar width (at $60d_{inlet}$) Vs Inlet Reynolds number

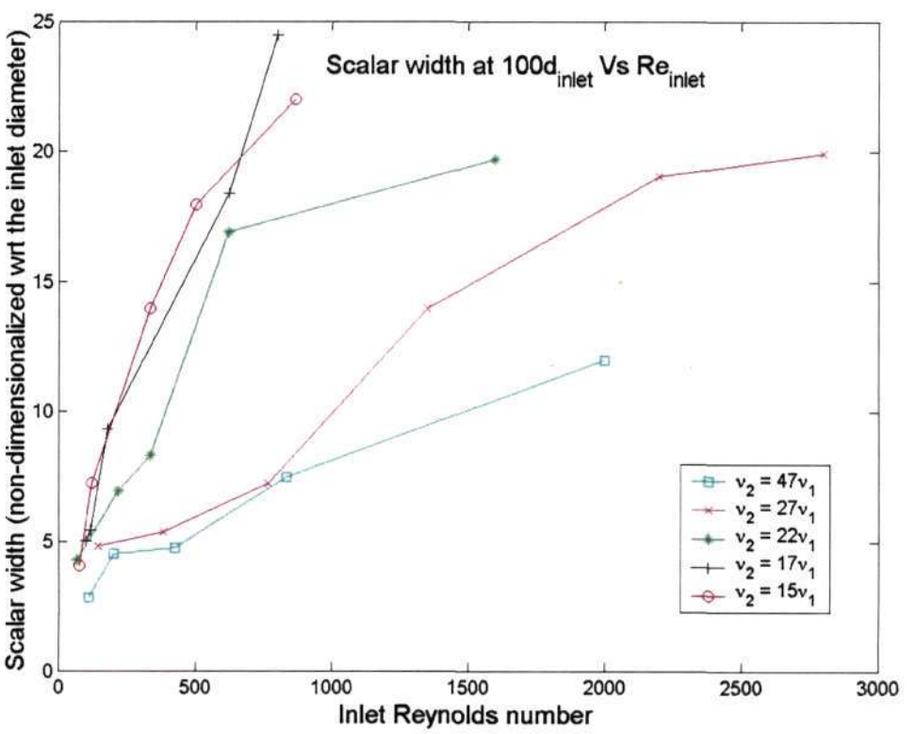

Figure 2.23: Scalar width (at $100d_{inlet}$) Vs Inlet Reynolds number

on this result, we decided to look into this issue more in detail using streak photography. The results are presented in section **2.6.2.**

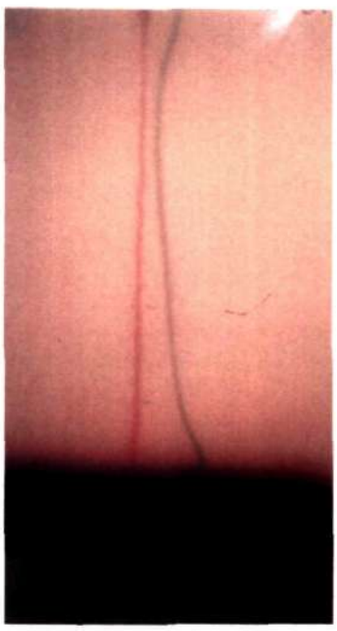

Figure 2.24: Scalar spread Vs Velocity spread
$Re_{inlet} = 1500$, $\nu_2 = 600\nu_1$

2.6.1.2 Entrainment through two different layers

In figure 2.25, we present a result indicating the behavior of the jet when it enters a high viscosity fluid after passing through a fluid of its own viscosity. The transition takes place at the interface indicated by the dark line in the figure. In the dotted box shown in the figure, small-scale fluctuations in the turbulent jet are evident. When it passes into the high viscosity region, all small-scale fluctuations are suppressed, however, small wave-number fluctuations still persist. In the higher-viscosity medium, the flow seems to have undergone a reverse transition (tending towards the laminar regime) resulting in lower entrainment.

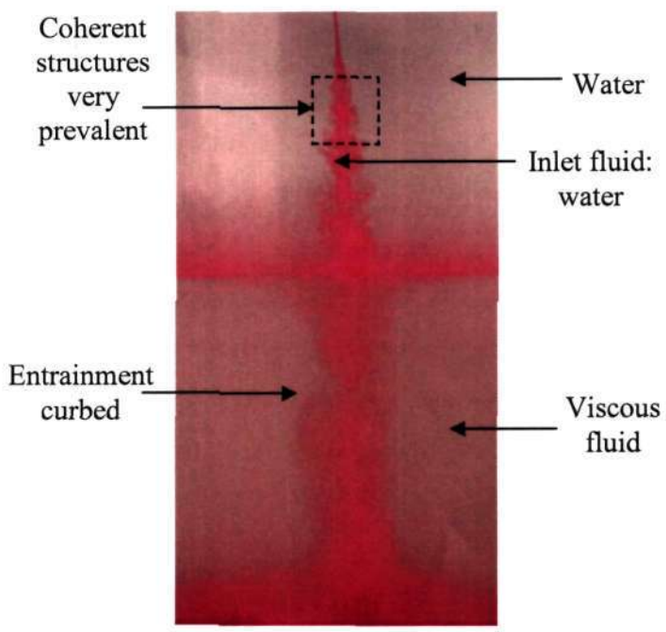

Figure 2.25: Entrainment through two different layers, $Re_{inlet} = 450$

2.6.2 Streak photography

As was discussed earlier, experiments were performed with the ambient fluid seeded with fine aluminium particles. Images taken with long exposures (8 – 15 s depending on the inlet Re and the viscosity ratio) are presented here. The streaks that are formed by the particles are indicative of the velocities in the flow. The inlet fluid is dyed with fluorescein dye and the scalar spread is indicated by the extent to which the green colour has spread.

Figures 2.26-2.29 are a set of images taken for a particular viscosity ratio ($\nu_2 = 78\nu_1$) and increasing inlet Reynolds number. It is very interesting to note that there is effectively an axial co-flow outside the main jet in the case of $Re_{inlet} = 267$. It is very evident that the axial momentum has spread to a much larger extent than the scalar (inlet fluid). This points towards an interesting result, which suggests that the scalar width (extent to which

the inlet fluid spreads) is very different from that of the velocity width (the extent to which the axial momentum has spread) in this case. Also to be noted is the fact that the turbulence level is very low in this case and the flow is almost fully laminar. Now, as we increase the inlet Reynolds number (figures 2.27-2.29), we observe the particles from the ambient fluid tend to travel into the main jet-flow rather than moving downstream alongside the jet, as in the case of $\mathbf{Re_{inlet} = 267.}$ As the inlet Reynolds number is increased, the turbulence level also goes up provided the viscosity ratio is the same. The velocities outside the main jet vary from being fully vertical (downwards) to fully horizontal (radially inward) as the inlet Reynolds number is increased from the flow being fully laminar to the flow being fully turbulent. To support this argument, an image from an experiment where the viscosity ratio is unity and the inlet Reynolds number high enough to ensure high levels of turbulence (and high levels of entrainment too) is presented in figure 2.30. It is very clear from this image that the outside ambient fluid is traveling radially towards the jet rather than flowing downstream alongside the jet. The velocity and the scalar widths are almost equal here.

The implications of the results from streak photography are quite important in any mixing studies. It is clear that even in cases where there is hardly any entrainment happening, the axial momentum can spread to a large extent. There will be no correlation between the velocity width and the corresponding entrainment. Hence, inferring on entrainment by measuring only the velocity width, as in the work of Agarwal. A and Prasad. A.K.[39], would be misleading. In any mixing studies, where the primary aim is to study the amount of mixing between the inlet and the ambient fluid, it is important to look at the scalar spread rates rather than the velocity counterparts. It is important to note that the term "entrainment" refers to the process of inducing flow in the ambient fluid and finally the mixing of the inlet and the ambient fluids.

Results from entrainment quantification (Sec. 2.5) have not been presented here. They also pointed towards all the qualitative conclusions that have been made based on the time-averaged images from which the scalar widths were obtained. It was difficult to obtain clean quantitative data because of various factors like the finite size of the main

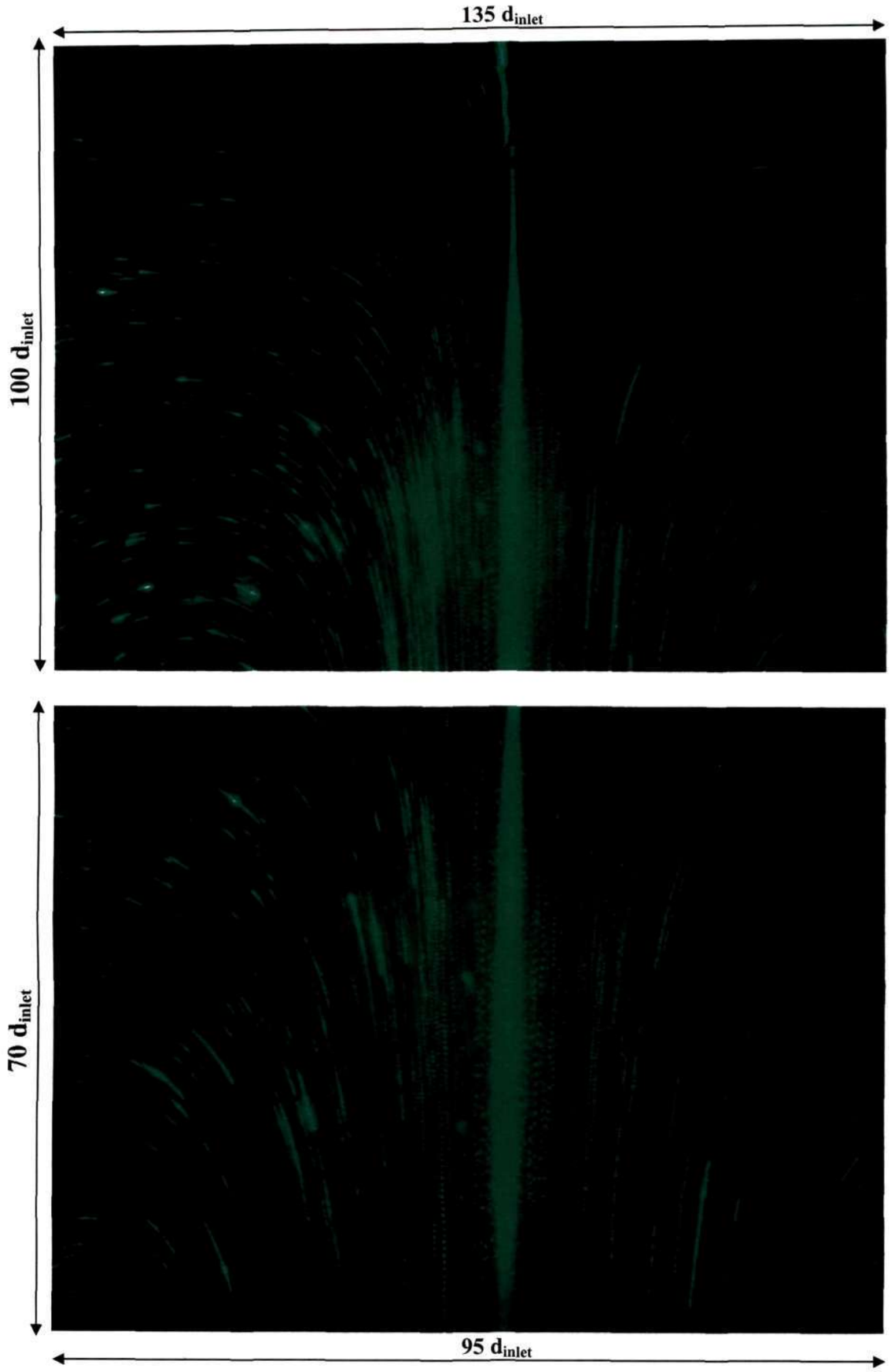

Figure 2.26: Entrainment completely suppressed, velocity width much greater than the scalar width. (Re_{inlet} = 267, $\nu_2 = 78\nu_1$)

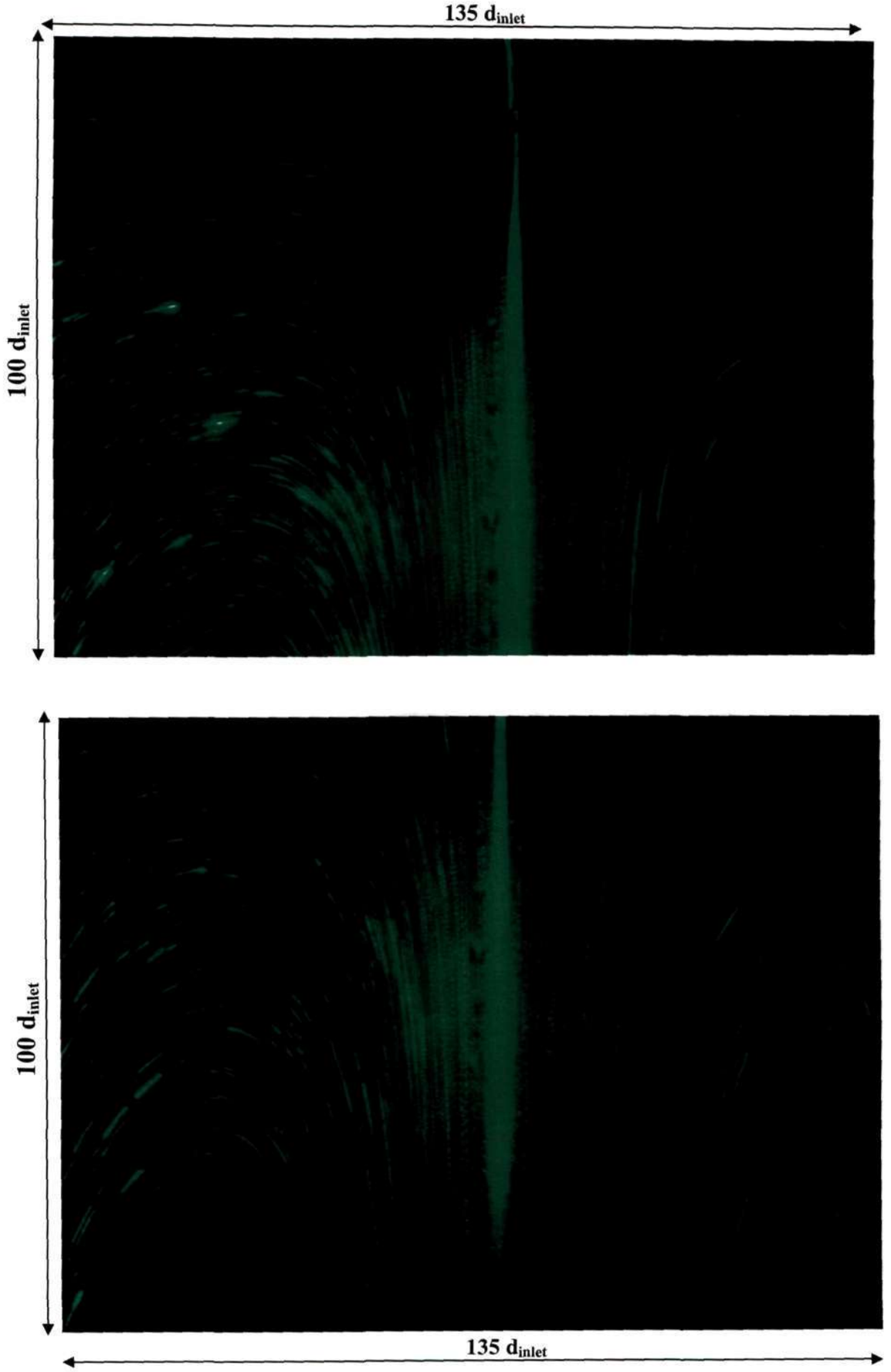

Figure 2.27: Velocity and Scalar widths, $Re_{inlet} = 566$, $\nu_2 = 78\nu_1$

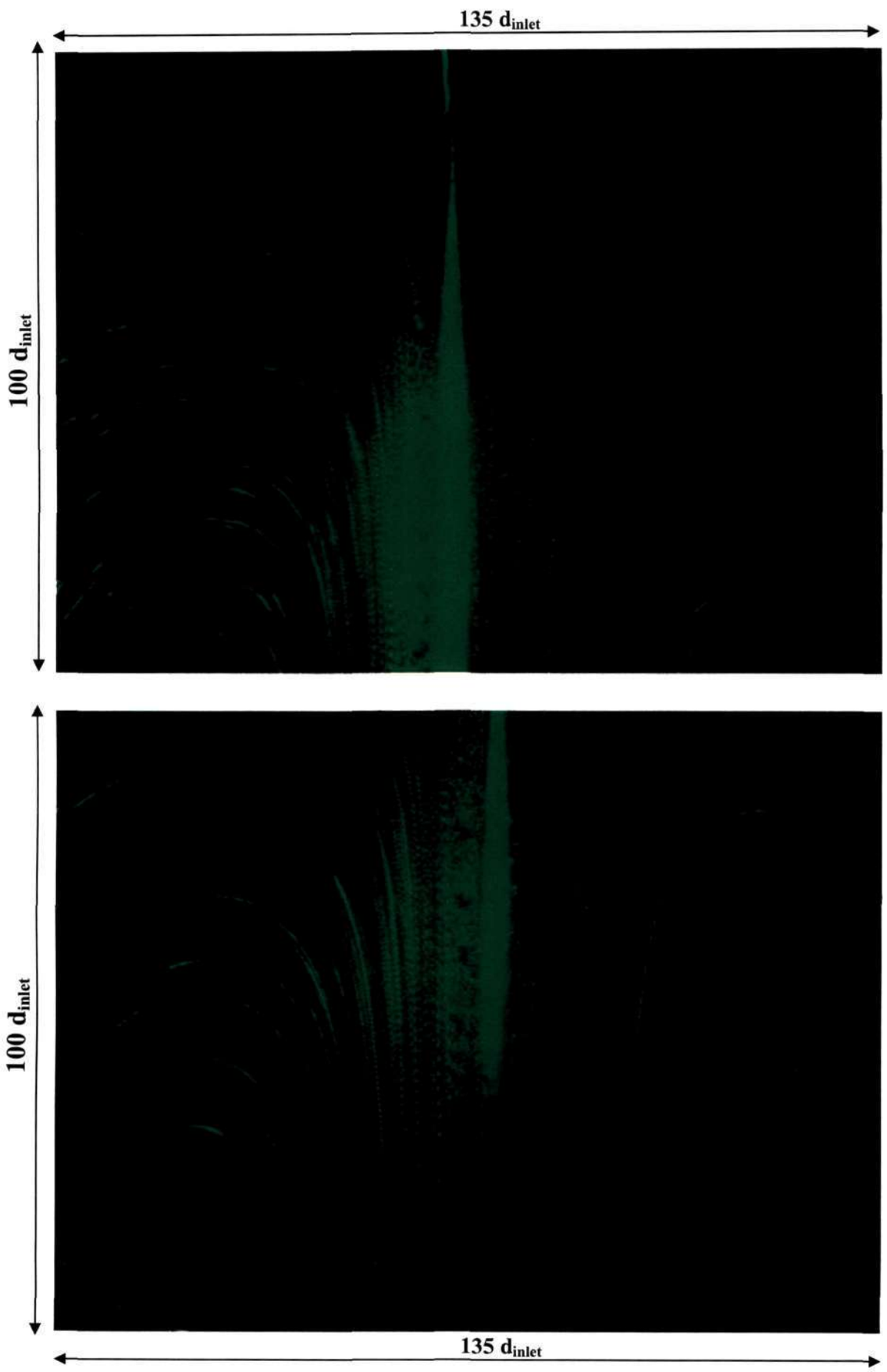

Figure 2.28: $Re_{inlet} = 1499$, $\nu_2 = 78\nu_1$

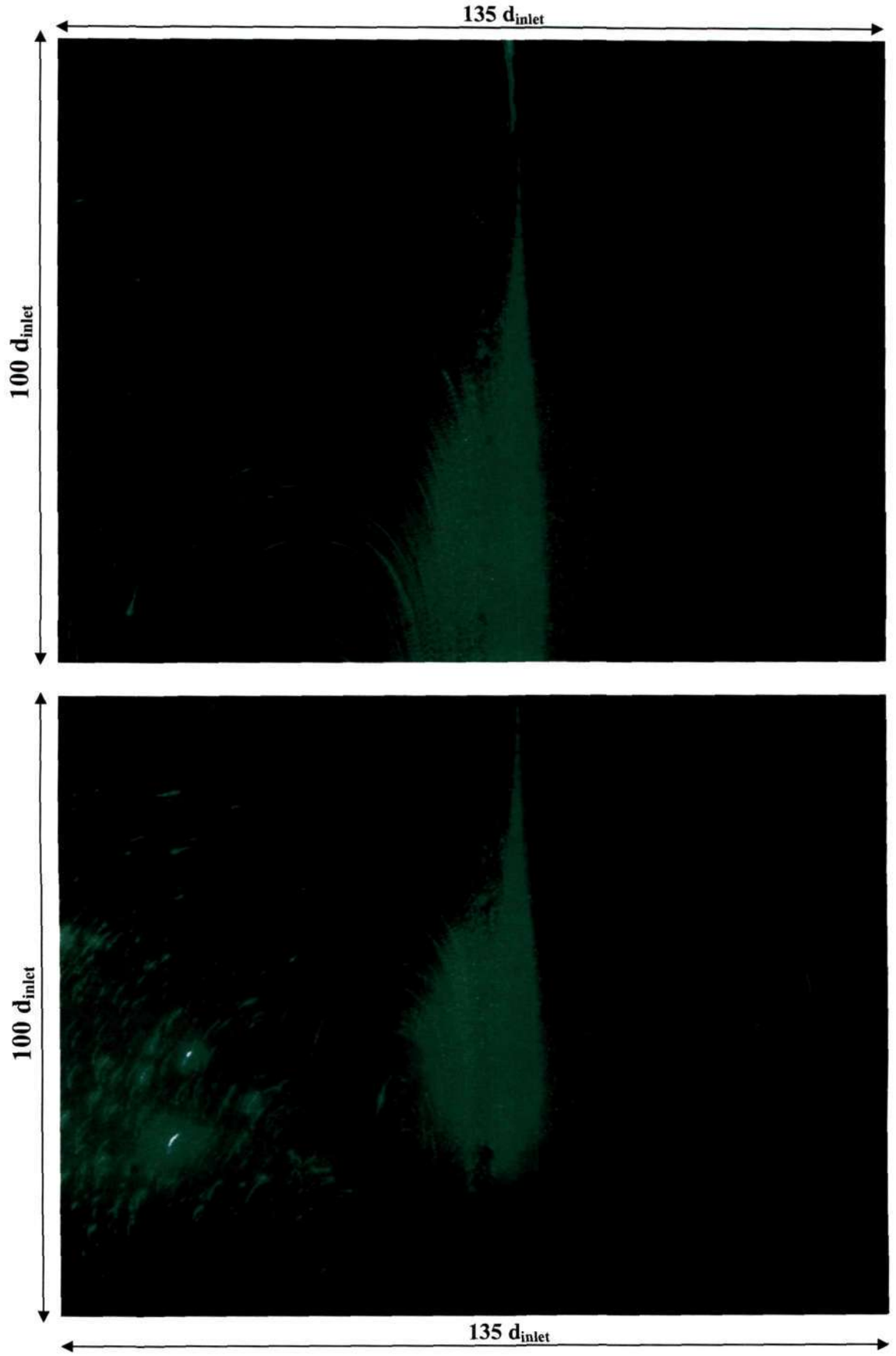

Figure 2.29: Velocity width approaching the scalar width (Re_{inlet} = 2848, $\nu_2 = 78\nu_1$)

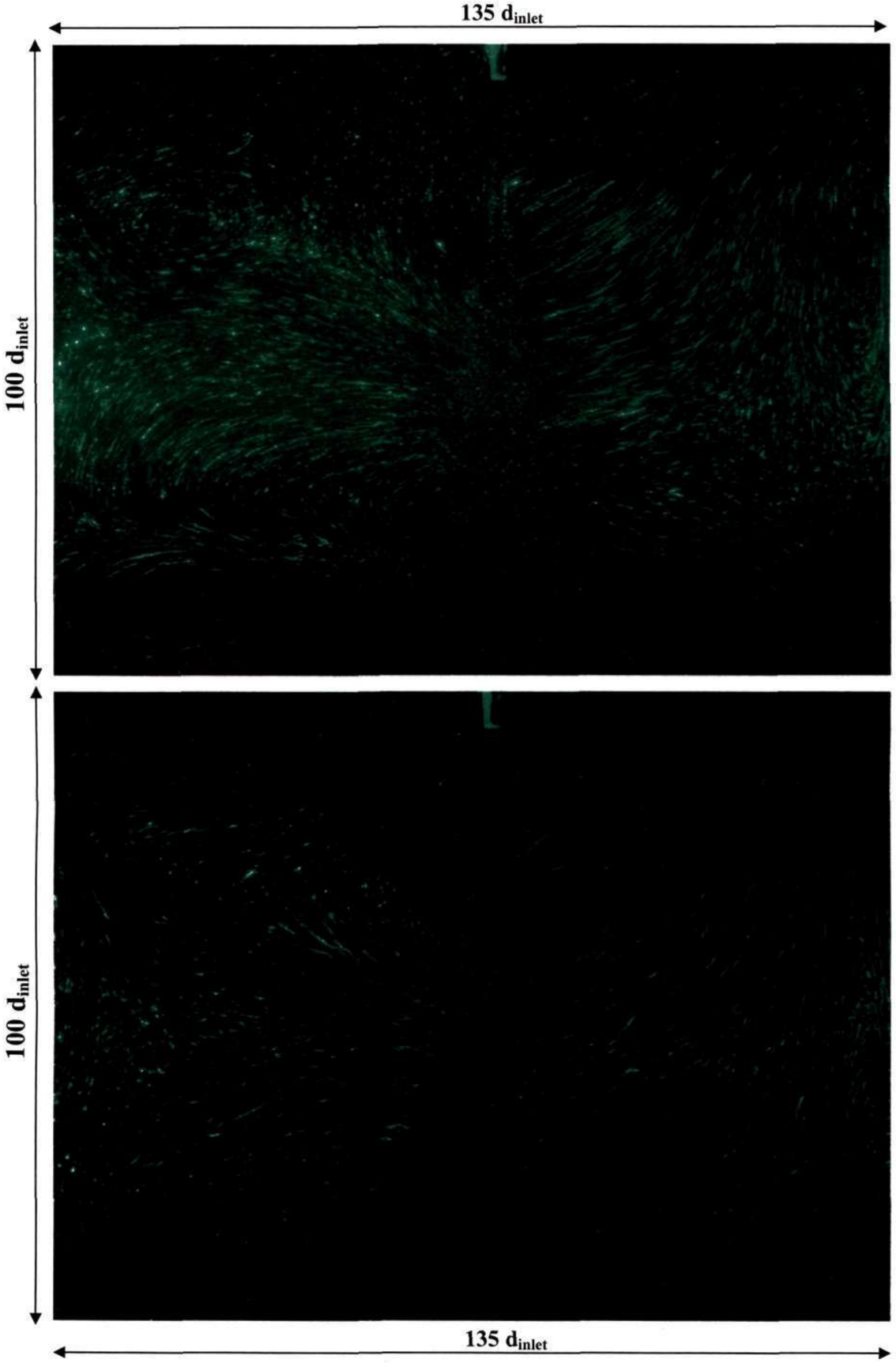

Figure 2.30: Velocity width equal to the scalar width. (Re_{inlet} = 350, $\nu_2 = \nu_1$)

glass tank (this would mean the jet does not travel through the same distance throughout the experiment), very small times before an appreciable coloured layer settles down in the case of fully-turbulent flow etc. However, the purpose of having a high-density bottom layer to result in a clean standard set-up was achieved in all the experiments.

Chapter 3

2-D Simulations using discrete vortex methods (DVM)

We have also addressed the same problem via 2-D simulations using vortex methods. A brief introduction to how vortex methods work is given below. Also, the advantages and disadvantages associated with DVM are discussed. A very detailed introduction to DVM can be found in [22, 23].

3.1 Introduction

DVM are numerical schemes that are based on the vorticity in the flow. The main reason to base the numerical method on the vorticity is that, typically, only a small portion of the flow contains vorticity. This can lead to significant savings in storage and computational effort. DVM compute the evolution of vorticity using a Lagrangian approach, in which the computational points (vortices) follow the motion of the fluid. Vortex methods for the simulation of incompressible flows correspond to a numerical approach with three fundamental features. First, the Navier Stokes or Euler equations are formulated in terms of vorticity and so the spatial discretization is carried out over the vorticity field instead of the velocity field. Second, making use of one of Helmholtz' theorems which states the correspondence of vorticity elements with material fluid elements, the computational vortex elements are Lagrangian and so convect with the fluid velocity. And third, to obtain the fluid velocity one makes use of the fact that the vorticity, defined as $\omega = \nabla \times \mathbf{u}$, can be inverted giving the velocity $\mathbf{u}$ as an integral over the vorticity field. This is the Biot-Savart law in vorticity kinematics, which allows to completely describe the flow field by tracking vorticity elements.

Describing the flow in terms of vorticity is desirable due to the intuitive power of visualizing the vorticity field, especially in complex and unsteady flows. Another advantage is the fact that the pressure drops out of the governing equation, and thus only needs to be solved for when and where force measurements are desired. In addition, as the DVM literature profusely extols, the fact that the vorticity field is predominantly

compact means that smaller-sized computational domains can be used, in comparison with primitive variable formulations, and also boundary conditions at infinity can be automatically satisfied. In contrast, satisfying the free-space boundary condition of external flows can be a delicate matter in grid-based with truncated flow domains. Furthermore, the Lagrangian vortex particles convect without numerical dissipation, as the non-linear term of the Euler or Navier-Stokes equations is traded by a set of ordinary differential equations for the particle trajectories. This is, again, in contrast with grid-based schemes, which inevitably suffer from numerical dissipation. Finally, the essential grid-free nature of the DVM is itself an advantage, as grid-generation is often one of the most expensive processes in computational fluid dynamics, CFD. The above stated advantages are most often critical for high Reynolds number flows. The difficulties that arise with DVM, on the other hand, will be discussed later.

3.2 Basic Formulation of DVM[22]

Let **u** (**x**, t) be the velocity field and **ω** (**x**, t) = ∇ x **u** (**x**, t) the vorticity field. Taking the curl of the momentum equation and considering an incompressible fluid for which ∇ . **u** (**x**, t) = 0, the vorticity transport equation is obtained. This is the governing equation in vortex methods, which for three-dimensional flow corresponds to the following vector equation,

$$\frac{\partial \omega}{\partial t} + u \cdot \nabla \omega = \omega \cdot \nabla u + \nu \nabla^2 \omega \qquad (3.1)$$

The assumptions in the above equation are: constant density flow, constant viscosity flow, conservative body forces, an inertial frame of reference and unbounded domain. In the case of a two dimensional and inviscid flow, the right hand side of (3.1) is zero and the governing equation reduces to the simple form $\frac{D\omega}{Dt} = 0$, where $\frac{D}{Dt}$ stands for the material derivative. This corresponds to the basic formulation of vortex methods, for which clearly a Lagrangian method based on elements of vorticity is natural and ideal. Based on this simplest of formulations, the vortex method historically found its first

successful applications in the simulation of phenomena governed by the 2D Euler equations. Subsequently, vortex methods have been extended to three-dimensional flow by including the vortex stretching/tilting term, and have incorporated the presence of internal boundaries by using vortex sheet formulations in the inviscid case and vorticity generation models with boundary elements for the viscous case. Viscous effects were added first by the random walk method[24], but a number of so-called deterministic viscous schemes have been proposed and tested during the last two decades.

In the vortex blob discretization, the elements are identified by a position vector, $\mathbf{x}_i$; a strength vector (vorticity x volume) of circulation; and a core size, σ_i. The discretized vorticity field is expressed as the sum of the vorticities of the vortex elements in the following way:

$$\omega(x, t) = \omega^h(x, t) = \sum_{i=1}^{N} \Gamma_i(t)\zeta_{\sigma_i}(x - x_i(t)) \tag{3.2}$$

where Γ_i corresponds to the vector circulation strength of particle i (scalar in 2D). In the blob version of the vortex method – in contrast to point vortices, the elements have a non-zero core size σ_i and a characteristic distribution of vorticity ζ_{σ_i}, commonly called the cutoff function. Frequently, the blob cutoff function is a Gaussian distribution and the core sizes are uniform ($\sigma_i=\sigma$), which means that in two dimensions one has

$$\zeta_\sigma(x) = \frac{1}{k\pi\sigma^2}\exp(\frac{-|x|^2}{k\sigma^2}), \tag{3.3}$$

where the constant k determines the width of the cutoff and is chosen by different authors as 1, 2 or 4. We have used k = 4 in our simulations.

In the majority of vortex methods (almost all), the Lagrangian formulation is expressed by assuming that the vortex elements convect without deformation with the local velocity. The velocity is obtained from the vorticity using the Biot-Savart law:

$$u(x,t) = \int(\nabla xG)(x - x')\omega(x',t)dx' = \int K(x - x')\omega(x',t)dx' = (k * \omega)(x,t) \tag{3.4}$$

where $K = \nabla x G$ is known as the Biot-Savart kernel, G is the Green's function for the Poisson equation, and * represents convolution. For example, in two dimensions the Biot-Savart law is written explicitly as

$$u(x,t) = \frac{-1}{2\pi} \int \frac{(x - x')x\omega(x',t)\hat{k}}{|x - x'|^2} dx' \tag{3.5}$$

For the customary case of an axisymmetric cutoff function $\varsigma = \varsigma(r)$, $r = |x|$, the velocity kernel can be obtained analytically. For the 2-D Gaussian blob with k = 1, one has

$$K_\sigma(x) = \frac{1}{2\pi r^2}(-y, x)(1 - \exp(-\frac{r^2}{\sigma^2})) \tag{3.6}$$

The formula for the discrete Biot-Savart law in two dimensions gives the velocity as follows,

$$u(x,t) = -\sum_{j=1}^{N} \Gamma_j K_\sigma(x - x_j) \tag{3.7}$$

Finally, the Lagrangian formulation of the (viscous) vortex method in two dimensions is expressed in the following system of equations:

$$\frac{dx_i}{dt} = u(x_i, t) \tag{3.8}$$

$$\frac{d\omega}{dt} = \nu\nabla^2\omega + B.C. \tag{3.9}$$

The complete numerical method is defined by Equations (3.8) and (3.9) which express that the method is to be implemented by integrating the particle trajectories due to the local fluid velocity, while the velocity is obtained from the vorticity using the Biot-Savart law. The vorticity field evolves due to the effects of viscosity, both in the free-stream and on the boundaries (no-slip condition denoted by B.C.). The viscous effects in the free-stream are enforced by one of a variety of viscosity schemes available for vortex methods (described in the next section), while the effects due to solid boundaries are traditionally accounted for by generation of vorticity implemented in a version of the boundary element method. This is based on the physical mechanism by which the solid wall is a source of vorticity that enters the flow, so a vorticity flux $\frac{\partial\omega}{\partial n}$ may be determined at the wall to satisfy the boundary condition of no-slip at the surface.[25]

3.3 Viscous Schemes for Vortex Methods

Vortex methods have long proved to be an effective tool for the approximation of solutions to the Euler equations, and have been used for decades in the simulation for both unbounded and bounded flows. In most applications of more than academic interest, however, the limitations of the inviscid approximation cannot be accepted. Unfortunately, it is not easy to implement a numerical solution of the diffusion term in the vorticity transport equation that is compatible with the Lagrangian formulation. This section examines the different schemes that have been introduced over the years to include viscous effects in vortex methods.

Majority of viscous vortex methods are based on the viscous splitting or the fractional step algorithm. Viscous splitting – sometimes called "fractional step" method – is in fact a particular case of the general technique of "operator splitting", and it is introduced to viscous vortex methods together with the random walk diffusion scheme by Chorin.[24] Convergence of the viscous splitting algorithm for the Navier-Stokes equations in an unbounded flow is proved in [26] and [27]. The algorithm consists of sub-time-steps where the effects of convection and diffusion are considered successively. More sub-steps are involved in higher order schemes, but the basic two-step viscous splitting algorithm is second-order accurate at each time step and first-order overall (irrespective of the time-stepping scheme used). For two-dimensional viscous flows,

$$\frac{\partial \omega}{\partial t} + u \cdot \nabla \omega = \nu \Delta \omega \tag{3.10}$$

Sub-step 1: Convection

$$\frac{\partial \omega}{\partial t} + u \cdot \nabla \omega = \frac{D\omega}{Dt} = 0 \begin{cases} \dfrac{dx_p}{dt} = u(x_p) \\ \dfrac{d\omega_p}{dt} = 0 \end{cases} \tag{3.11}$$

Sub-step 2: Diffusion

$$\frac{\partial \omega}{\partial t} = \nu \Delta \omega \begin{cases} \dfrac{dx_p}{dt} = 0 \\ \dfrac{d\omega_p}{dt} = \nu \Delta \omega(x_p) \end{cases} \tag{3.12}$$

The convective sub-step in a vortex method is ideally expressed in the Lagrangian frame of reference, the same as for an inviscid flow. Using the discrete representation of the vorticity field, the velocity is obtained by the Biot-Savart law and the particles are advanced in the inviscid sub-step. But the discretization of the vorticity field in vortex methods, conceived for the simulation of the inviscid vorticity equation, is not well suited for the evaluation of the Laplacian in the diffusive term, because of the unstructured nature of the data. Hence a wide variety of approaches have been put forward to include diffusive effects in a vortex method.

The random vortex method (RVM) was introduced by Chorin[24] and is formulated essentially as a fractional step method. It takes into account the viscous effects in the mean, simulating diffusion by a random walk, i.e., a Brownian-like motion of the vortex particles. Consider the discretized vorticity as expressed by (3.2); in the inviscid case the particle strengths Γ_i remain constant, and ς is not a function of time, i.e. the vortices are elements of fixed geometry, and the particle positions are updated only as a result of convection. The random vortex method acts by modifying the positions of the particles at each (diffusive sub-) step by adding a random walk, that is, the particle locations are transformed using: $x_i^{n+1} = x_i^n + \xi_i^n$, where the ξ_i^n are Gaussian independent random variables of zero mean and variance equal to $2\nu\Delta t$. This formula is based on the probabilistic interpretation of the diffusion equation, which says that the probability of finding a particle that moves at random in Brownian motion is given by (3.12). The main disadvantage is that it requires a large number of particles to obtain reasonable accuracy, due to its slow convergence rate. Also, only slightly viscous flows can be modeled, and at low Reynolds numbers the solution can be quite rough. Generally, the (lower) limit is taken as Re = 100.

Some of the other viscous diffusion schemes that have been suggested are Particle Strength Exchange (PSE), Redistribution Method, Fishelov Method, Diffusion Velocity Method and the Core Spreading model. Owing to reasons like requirement of large computational powers, lower accuracies involved and loss of the grid-less nature of DVM, we decided not to look into the usage of RVM, PSE, Redistribution and Fishelov methods for our problem where viscosity is varying in space. A more detailed description of all the above viscous schemes is given in [22].

3.3.1 Diffusion Velocity

The diffusion velocity approach[28] can be deduced from considering the general case of an arbitrary scalar function in two space dimensions F(x,y,t) that moves with velocity **u**(x,y,t) = (u,v), whose evolution equation can be written as

$$\frac{\partial F}{\partial t}+\frac{\partial (uF)}{\partial x}+\frac{\partial (vF)}{\partial y}=0 \tag{3.13}$$

The two-dimensional vorticity transport equation (3.10) can be written in this form, using the incompressibility condition,

$$\frac{\partial \omega}{\partial t}+\frac{\partial}{\partial x}[(u-\frac{\nu}{\omega}\frac{\partial \omega}{\partial x})\omega]+\frac{\partial}{\partial y}[(v-\frac{\nu}{\omega}\frac{\partial \omega}{\partial y})\omega]=0 \tag{3.14}$$

Comparing (3.13) with (3.14), where (u, v) is the convective velocity, the diffusion velocity is defined by the extra contribution to the total velocity, as follows,

$$u_d=-\frac{\nu}{\omega}(\frac{\partial \omega}{\partial x},\frac{\partial \omega}{\partial y}) \tag{3.15}$$

so that the vorticity equation can now be written in a conservation from as

$$\frac{\partial \omega}{\partial t}+\frac{\partial}{\partial x}(\omega(u+u_{dx}))+\frac{\partial}{\partial y}(\omega(v+u_{dy}))=0 \tag{3.16}$$

The concept of a diffusion velocity implies that the net flow of vorticity is proportional to the vorticity gradient, which is analogous to Fick's law of diffusion where ν/ω is taken as a non-constant diffusion coefficient. It translates into saying that ω as a preferred direction of transport, namely that of $\nabla\omega$. The way the vorticity gradient is obtained in

the diffusion velocity method is by directly taking the derivatives of the cutoff function in the discretized vorticity representation. The suitability of the diffusion velocity concept was demonstrated in [28] for a one-dimensional diffusion test problem and for the case of a circular cylinder at Re = 1200 and Re = 40. However, the results presented for cylinder flow are of rather low resolution when compared with finite-difference calculations.

Comparing equations (3.13) and (3.14) and obtaining an expression for the diffusion velocity is equivalent to equating the solutions of the two differential equations. The solutions can very well be different by the gradient of an arbitrary scalar potential, satisfying the two equations at the same time. No specific reason has been given by the authors in [28] for why the gradient of this arbitrary potential should always be zero. Even though it seems to work well for some specific situations, the physical basis for the method does not seem to be convincing. We have got satisfactory results with the above method for a jet where the viscosity does not vary in space. As will be shown later, when the viscosity is varying in space, the method is not appropriate.

Kempka and Strickland[29] have suggested some modifications to the diffusion velocity model to account for the non-solenoidal nature of the diffusion velocity that Ogami and Akamatsu[28] have used. A formulation that relates the area expansion of a blob to the diffusion velocity divergence is presented. Accurate simulations of the one-dimensional diffusion equation are obtained. The method has not been tested out for other more complex situations. Also, no justification to why the gradient of an arbitrary scalar potential (as explained in the earlier paragraph) in deriving the expression for the diffusion velocity is given.

3.3.2 Core Spreading

During the early1990's, only two viscous vortex methods were well known: the random vortex method of Chorin[24] and core spreading, which apparently was used for the first time in [30]. The latter method was, however, under discredit due to the mathematical objections of Greengard.[31] Then, a correction was suggested for the core spreading

method by Rossi[32], and interest in this scheme was revived, but still only a very few workers have performed further investigations with it.

The core spreading method, presented by Leonard in [33], is a purely Lagrangian scheme that accounts for viscous effects by changing the *core size* of the particles to exactly solve the diffusion equation. It is easily understood using as analogy the classical exact solution of the two-dimensional Navier-Stokes equations termed "spreading line vortex"(see Batchelor[34], p. 204). In this problem the vorticity is given by

$$\omega(x,t) = \frac{\Gamma}{4\pi\nu t}\exp(-\frac{|x|^2}{4\nu t}) \tag{3.17}$$

Consider again the approximate vorticity given by the discretized form (3.2), but write it slightly differently to express the fact that the core function will now carry the dependence on time,

$$\omega(x, t) = \omega^h(x, t) = \sum_{i=1}^{N} \Gamma_i(t)\zeta_t(x - x_i(t)) \tag{3.18}$$

The core function is now chosen to be the solution of the heat equation with initial data ζ_0

$$\zeta_t(x) = \frac{1}{4\pi\nu t}\int e^{-(x-y)^2/4\nu t}\zeta_0(y)dy = (G * \zeta_0)(x), \tag{3.19}$$

where G is the heat kernel. If the initial distribution function ζ_0 is a Dirac delta, then

$$\zeta_t(x) = \frac{1}{4\pi\nu t}e^{-(x)^2/4\nu t} \tag{3.20}$$

By comparing with (3.17), the discretized vorticity field in two dimensions can be seen as a superposition of "spreading line vortices" of different circulation strengths. The core spreading vortex method is then formulated so as to satisfy identically the viscous part of the vorticity equation by expanding σ^2 linearly according to

$$\frac{d\sigma^2}{dt} = 4\nu \tag{3.21}$$

which means that the core of each particle must spread out at a rate proportional to $\sqrt{\nu t}$ or $\sqrt{\nu\Delta t}$ at each time step. As we use a Gaussian blob function with k = 4, the method is expressed in the following simple algorithmic rule:

$$\sigma_i^2(t+\Delta t) = \sigma_i^2(t) + \nu\Delta t, \quad \text{i} = 1.....\text{N} \tag{3.22}$$

The attraction of this formulation – apart from its utter simplicity of implementation – is that the method is fully localized and grid-free in nature (hence more easily expressed in a parallel application code), and that it is fully deterministic (so allows faster convergence and better error control compared with the RVM). Additionally, a core spreading scheme does not necessarily rely on the fractional step method. However, as mentioned, research in its regard was largely stalled when the method was declared inconsistent in 1985.[31], and it was proved that the scheme converges to an equation different from the Navier-Stokes equations.

The inconsistency of the core spreading method is related to the treatment of the particles as solid bodies, from which the "convection error" arises. With the core spreading method the diffusion of vorticity is approximated accurately, but the vorticity is advected with an average velocity and not with the actual local velocity. The vorticity is incorrectly convected even in the limit of infinitely many particles. Greengard derives in his note [31] the actual equation which is solved by the vorticity obtained by core spreading, which differs from the Navier-Stokes equation in the convection term only. But it is easy to understand the problem with a simple argument, noting that with the uncorrected method particle cores will grow to a size of at least $\sqrt{\nu T}$ in a simulation ran to a final time T. As the convergence of a vortex method depends on core size remaining small, the method will clearly eventually break down. This simple argument illuminates how a correction is implemented, based on adding spatial refinement, e.g., splitting of the blobs, which have grown beyond a specified maximum into smaller elements. Rossi[32] proved the convergence of the corrected core spreading method with vortex splitting and provided details of implementation. He went on to propose vortex merging as a means to control problem size[35], as the splitting can rapidly increase the blob population. The vortex splitting scheme of Rossi is described in Section (3.3.3).

3.3.3 Vortex splitting and merging

As said earlier, a basic core spreading vortex scheme is inconsistent and the splitting algorithm controls the consistency error by maintaining small vortex core sizes. [32] In order to maintain small blob sizes throughout the simulation, the basic core-spreading scheme is coupled to spatial refinement. The refinement process splits any blob wider than l into a configuration of thinner blobs of width less than l. The numerical parameter $\alpha \in [0,1]$ controls the accuracy and stability of adaptive spatial refinement. The refinement process will approximate a single vortex element having width l with several blobs of width αl. Therefore, a refinement algorithm takes all vortex elements with core sizes greater than or equal to l and splits them into many, each of which is scaled by a factor of α.

The particular refinement process is somewhat arbitrary. Here, only 1-4 refinement, where one blob splits into four, is explained, but this can be carried out for any "refined" configuration. The general strategy is to conserve as many moments as needed to constrain the free variables. To begin, a single vortex element with circulation γ and variance σ^2 will split into four identical vortices, each with a variance of $\alpha^2\sigma^2$. Without loss of generality, one can assume the original vortex is located at the origin. Conservation of the zeroth moment indicates the obvious: the new vortices must have the same circulation. Conservation of the first moment along with the rotational symmetry of the system requires that each vortex have circulation $\frac{\gamma}{4}$ and be centered uniformly along a circle of radius r. Conservation of the second moment constrains the last variable

$$r = 2\sigma\sqrt{1-\alpha^2} \tag{3.23}$$

Now, all of the free parameters of 1-4 refinement have been determined, and it is possible to explicitly describe the algorithm.

1. Approximate the exact initial vorticity distribution with vortex elements.
2. Implement the basic core-spreading algorithm to convect and diffuse the vortex blobs.

3. Split any element with $\sigma_i > l$ according to 1-4 refinement process listed above with the refinement radius described in equation (3.23).
4. Repeat (2) and (3) until reaching time T.

Rossi[35] has suggested the process of merging groups of many Gaussian basis functions into a single basis function in vortex simulations. This is performed to account for the large computational efforts demanded by the increase in the number of blobs while implementing the vortex-splitting algorithm. Nearly overlapping computational elements can be expressed more simply as a single element in certain situations, reducing the computational load while maintaining the same accuracy.

Numerical merging will consist of replacing a collection of vortex elements with a single element. From the N computational elements, a subset $(\gamma_{ij}, \vec{x}_{ij}, \sigma_{ij})$ for $1 \le j \le n$ shall be merged into a single element. The postmerger element will be labeled 0 and the subindices *ij* will be dropped because only the n elements to be merged are of importance here. It is necessary to assume that all $\gamma_i's (1 \le i \le n)$ have the same sign. Numerical merging conserves the zeroth, first and second moments of vorticity. This effectively defines the numerical merging process because these constraints determine the strength, position and width of the postmerger element:

$$\gamma_0 = \sum_{i=1}^{n} \gamma_i \tag{3.24}$$

$$\gamma_0 \vec{x}_0 = \sum_{i=1}^{n} \gamma_i \vec{x}_i \tag{3.25}$$

$$4\gamma_0 \sigma_0^2 = \sum_{i=1}^{n} \gamma_i (4\sigma_i^2 + |\vec{x}_i - \vec{x}_0|^2) \tag{3.26}$$

Maintaining $l_m \le \sigma_i \le l_M$ is necessary to maintain accuracy in the evolution of the computational field relative to the exact solution. Choice of which blobs are to be chosen for merging, l_m and l_M are based on minimizing the difference in the vorticity fields before and after the merging event:

$$e(\vec{x}) = \frac{\gamma_0}{4\pi\sigma_0^2}[\exp(-\frac{|\vec{x}|^2}{4\sigma_0^2}) - \sum_{i=1}^{n} \frac{\gamma_i}{\gamma_0}\frac{\sigma_0^2}{\sigma_i^2}\exp(-\frac{|\vec{x}-\vec{x}_i|^2}{4\sigma_i^2})] \tag{3.27}$$

The goal is to choose efficiently a collection of vortices together with the parameters $(\gamma_0, \vec{x}_0, \sigma_0)$ so that this error is small. More details can be found in [35].

3.4 Fast Multipole Expansion

For convection of the vortices, the velocity field can be found from the Biot-Savart law. Such a velocity field implicitly satisfies mass conservation. However, the computational effort required to evaluate it directly is high; it is proportional to the square of the number of vortices. Fast algorithms have been developed to do it with much less effort. Clarke and Tutty[36] have suggested a zonal decomposition/summation method, which is explained below.

The zonal decomposition method relies on the following theorem:

Suppose there are N_P vortex blobs contained within a domain D, then sufficiently far from D, the velocity induced by all N_P vortices can be calculated using a Laurent series in n_t terms (where n_t depends only on the accuracy required). 'Sufficiently far' in this case turns out to be relative to the maximum distance from any vortex in D (this maximum distance is termed the 'radius' of a zone). The coefficients of the Laurent series can be calculated in advance of the summation relative to the arbitrary center point 'λ'. Hence, beyond a certain distance from the center, we can use this series and, if N_P is large, save work compared to a direct summation over each vortex. The formulae for the coefficients, velocity and convergence condition are:

Let $$\alpha_K = \sum_{j=1}^{N_P} \Gamma_j (Z_j - \lambda)^{(K-1)} \tag{3.28}$$

then $$u(z) - iv(z) = \frac{1}{2\pi i}\sum_{K=1}^{n_t} \alpha_K (Z-\lambda)^{-K} + O(\varepsilon) \tag{3.29}$$

provided $$|Z-\lambda| > h(n_t, \varepsilon).\sup\{|Z_j - \lambda| : j = 1...N_P\} \tag{3.30}$$

where α_K are the coefficients for the zone, Γ_j and Z_j are respectively the strengths and positions of the vortices in the zone, λ is the (complex) center point of the zone and h is a function depending on n_t, the number of terms used in the series, ε, the accuracy required and sup, the supremum function.

To use the theorem effectively, it is necessary to construct an algorithm to decompose the entire vortex field into a set of zones. In our simulations, the boxes were constructed in the following way. Consider a section that extends to infinity on either side in the lateral direction normal to the axis. Its width was chosen to be equal to that of the inlet diameter and that specifies its local width. The first section starts right from the exit of the inlet pipe. Boxes of size equal to the local width are constructed within the section till the last vortex particle in the section is captured within a box. For the next section, the local width is chosen as 1.04 times the local width of the previous section. This is done to account for the vortex particles spreading in the lateral direction (resulting in lesser number of particles per unit area at an axially farther location). Sections (and then boxes within them) are constructed till the all the vortex particles in the computational domain are accounted for.

The arithmetic mean of the co-ordinates of the vortex blobs within a box is taken as the co-ordinates for the center of the box. The distance between the vortex blob (within the box) that is farthest from the center of the box and the center of the box is computed as the radius of the box. The parameters n_t and ε are chosen such that the maximum error induced by the method is within 1 percent (This is done by comparing the vorticity data computed via direct summation and by fast multipole expansion). If the number of particles within a box is less than or equal to N_{min} (say 7), direct influence of all the particles within the box is computed irrespective of whether the convergence condition (3.30) is satisfied or not. Typical construction of the boxes with the vortex particles is shown in figure 3.1.

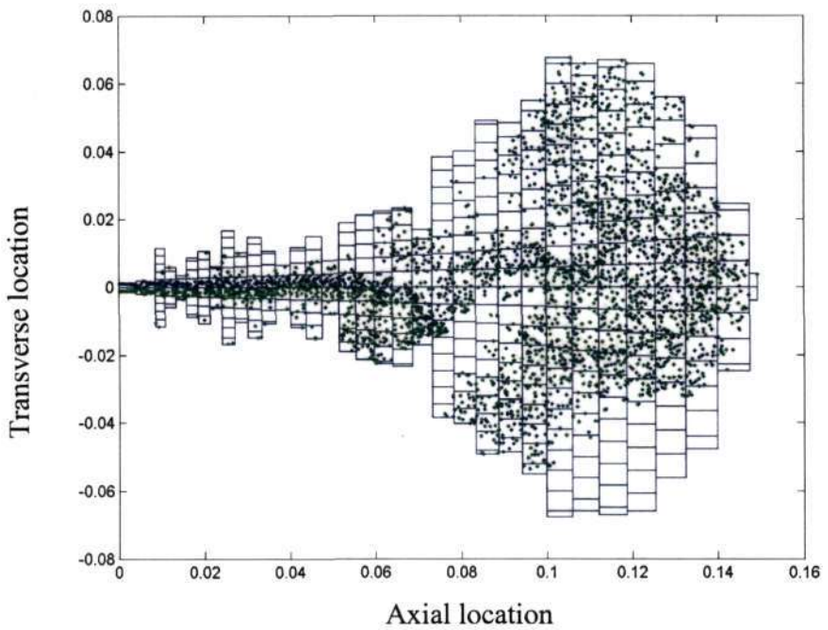

Figure 3.1: Fast multipole expansion, Number of particles = 1700

3.5 Viscosity-stratified flows

The two-dimensional vorticity form of the Navier-Stokes equations for a flow in which the viscosity is varying in space is as follows:

$$\rho\left(\frac{\partial \omega}{\partial t}+u\frac{\partial \omega}{\partial x}+v\frac{\partial \omega}{\partial y}\right)=\mu\frac{\partial^2 \omega}{\partial x^2}+2\frac{\partial \mu}{\partial x}\frac{\partial \omega}{\partial x}+\mu\frac{\partial^2 \omega}{\partial y^2}+2\frac{\partial \mu}{\partial y}\frac{\partial \omega}{\partial y}+$$
$$2\frac{\partial^2 \mu}{\partial x \partial y}\left(\frac{\partial v}{\partial y}-\frac{\partial u}{\partial x}\right)+\frac{\partial^2 \mu}{\partial x^2}\left(\frac{\partial u}{\partial y}+\frac{\partial v}{\partial x}\right)-\frac{\partial^2 \mu}{\partial y^2}\left(\frac{\partial u}{\partial y}+\frac{\partial v}{\partial x}\right) \tag{3.31}$$

where ρ is the constant density, u the x-component of the velocity vector, v the y-component of the velocity vector (x being the axial direction in our simulations), μ the dynamic viscosity and ω the vorticity.

The main difficulty in implementing vortex methods for a flow governed by (3.31) is that, viscous splitting (Sec 3.3) is not an obvious choice as terms containing the

derivatives of viscosity, velocity components and vorticity together exist. It is not possible to explicitly split the equation into convection and a diffusion part.

3.6 Simulation Method

In this section, the procedures adopted to run our simulations for a viscosity-stratified case are presented. Two sheets of vorticity represent an inlet slot of width **D** and length $\mathbf{P_L}$, through

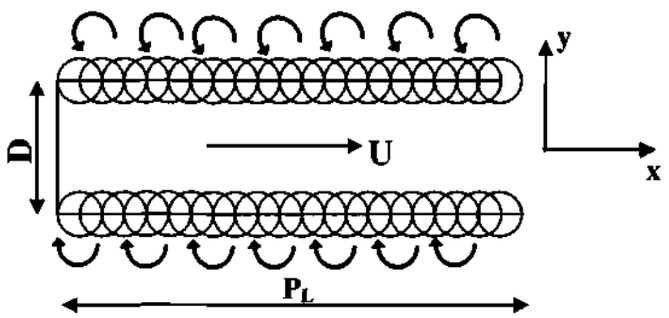

Figure 3.2: Vortex blobs at the inlet

which a fluid is flowing at constant speed **U**. The finite-sized vortex blobs have an overlap of around 50 %. Figure 3.2 represents the vortex blobs on the inlet pipe, with the circular arrows indicating the sense of rotation of the top and the bottom row of vortices. The sizes and the overlap are chosen such that the errors in the velocity profile at the centerline of the inlet pipe are within 1 %. The strengths of the blobs are evaluated as follows:

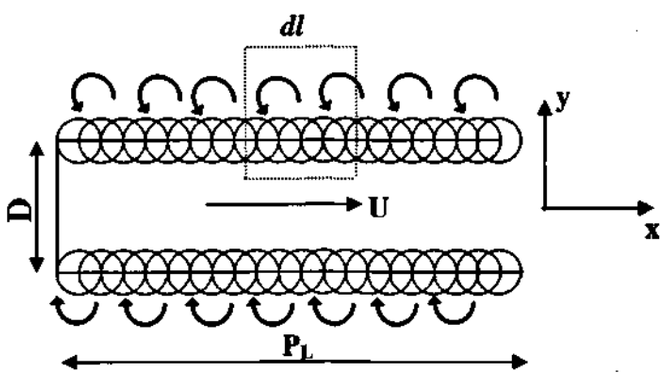

Figure 3.3a

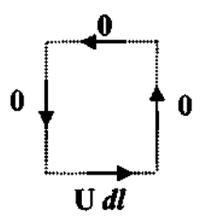

Figure 3.3b

Zooming in on the box (of size ***dl x dl***) drawn with dashed lines in the figure **3.3a**, we compute the total circulation around the box. As indicated in the figure **3.3b**, the circulation comes out as **U** ***dl***. The circulation in the box, γ = **U** ***dl*** and hence the circulation per unit length (γ/ ***dl***) = **U**. The circulation strength of each of the vortex blob should therefore be $\mathbf{UP_L/N_P}$, where N_P is the number of vortex blobs representing the inlet pipe.

The inlet fluid is represented by a set of concentration particles (represented in the simulations via Gaussian basis functions, similar to the vortex blobs representing the

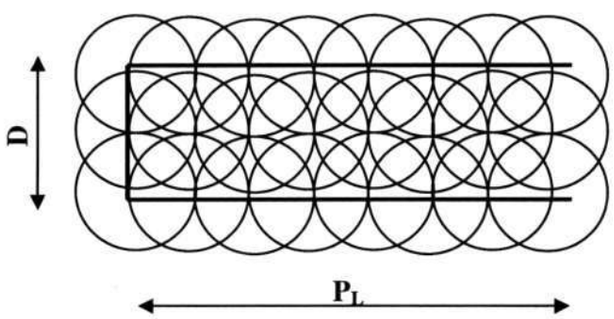

Figure 3.4: Concentration particles at the inlet

vorticity distribution). The concentration particles, which are passive scalars, represent the inlet fluid concentration in the entire flow-field. The blobs occupy the entire inlet pipe. The strengths and the overlap of these scalar particles are chosen such that the value of the concentration evaluated at any point inside the inlet pipe by adding up the influence of each and every scalar particle, is unity. This means that a concentration value greater than or equal to unity indicates the presence of the inlet fluid only and a zero value indicates the presence of the ambient fluid only. Figure 3.4 depicts the inlet scalar particles occupying the entire pipe, with around 50 % overlap. Particularly large sizes have to be chosen for the scalar particles so that the number of particles needed to represent the concentration field does not become huge. The value of the concentration evaluated at a point in space is what that decides the local viscosity value. A tan-hyperbolic function varying from ν_1 (the inlet fluid viscosity) to ν_2 (the ambient viscosity) as the concentration varies from 1 to 0 is used to map the concentration values onto corresponding viscosity values.

At the end of every time step, vortex blobs and concentration particles are pushed out of the inlet pipe into the ambient fluid with the inlet velocity U. The particles in the ambient fluid are convected with the Biot-Savart law velocity and the viscous diffusion scheme discussed below is used to expand the areas of all the vortex blobs.

As said earlier, the diffusion velocity model seems to work reasonably well for the case where the viscosities of the inlet and the ambient fluid are equal. Since the physical basis for the method is not very clear, an extension of the model to viscosity-stratified flows was not possible. In our simulations, we have used the core-spreading approach along with the corrections suggested by Rossi[32] by performing vortex splitting. The rate at which the area of a vortex blob increases is proportional to the value of the viscosity at the point in space where the blob's center lies. Even though, this does not account for all the terms containing viscosity derivatives in the vorticity equation, we believe that the errors will not be huge if the blobs are small enough and the derivatives of viscosity not too large. The derivatives are not completely neglected either, as the local viscosity values (which are varying in space) are what are used for implementing the viscous diffusion part. The concentration particles are treated as passive scalars and this means that the diffusion of concentration is not accounted for. The scalar particles are convected after every time step with the velocity computed at their centers using the Biot-Savart law. Figure 3.5 represents the way the vortex blobs and the concentration particles are convected and diffused at every time step. $\mathbf{U_C}$ is the convective velocity computing using the Biot-Savart law.

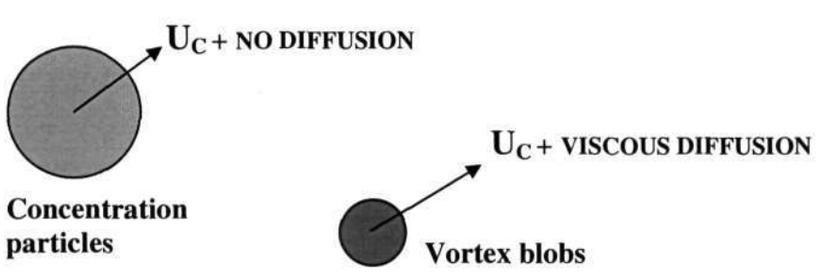

Figure 3.5: Concentration and Vortex particles

The fast multipole expansion algorithm is implemented to reduce the computational efforts from $O(N^2)$ to O(NlogN).[36] Vortex merging is implemented to account for the huge increase in the number of blobs caused by the vortex splitting technique. Randomness within 1% is forced onto the strengths of the blobs that enter the ambient fluid, as a means to simulate a real-life situation, which cannot be absolutely disturbance-free. This will also ensure that the flow is not perfectly symmetric about the x-axis. Blobs that have reached an L/D ratio of 160 or beyond are accelerated further by artificial forcing to ensure that they don't accumulate at the end and cause errors and difficulties in the simulations.

3.7 Results

3.7.1 Viscosity ratio = 1.0

In this section, the results obtained for a case where the inlet Reynolds number and the viscosity ratio (ν_2/ν_1) are 2000 and unity respectively, are presented. The inlet Reynolds number is high enough for the flow to be fully turbulent. No scalar particles are used, as the viscosity is uniform in space.

Figure 3.6 shows the instantaneous vorticity distribution of the fully turbulent jet. Interesting to observe is the fact that the initial laminar region (where the entrainment is also negligible) seems to be depicted well be two thin sheets of vorticity of opposite signs. The importance of the presence of a coherent structure at an axial location (which will in turn mean a net non-zero value of vorticity integrated radially over the entire axial location) in inducing entrainment at that location will be discussed in the final chapter. Fine coherent structures are also evident in this plot. The role of coherent structures of smaller wavelengths in the entrainment process will be discussed in the next chapter.

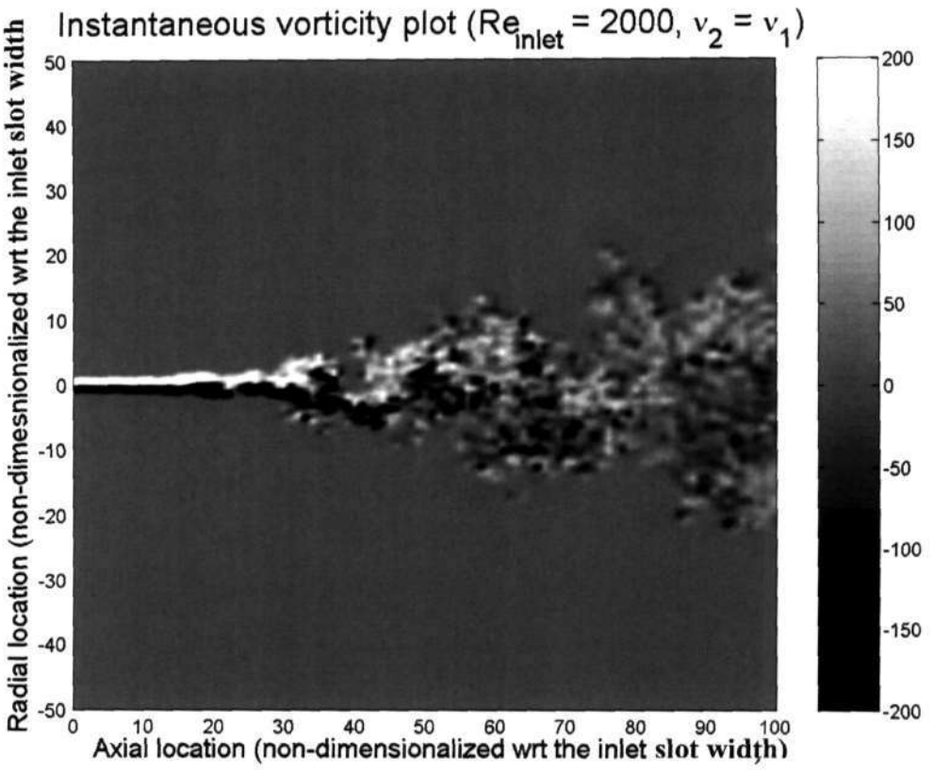

Figure 3.6: Instantaneous vorticity distribution

In figure 3.7, we show the variation of the (1/e) velocity width with the axial location. The jet being fully turbulent, the velocity and the scalar widths are expected to be comparable, as observed from our experiments. We observe that the variation switches from a straight line of one slope to another. The initial 20-30 **d** (**d** is the inlet slot width) is in the laminar regime, and hence we observe the slope to be small, as hardly any entrainment happens here. Now, as the flow undergoes a transition from the laminar regime to the self-similar turbulent regime, we observe the velocity spread rate to become much higher (owing to rapid entrainment) and hence resulting in a larger slope for the straight line. This larger slope is in good agreement with the findings of Fischer.[10]

In figure 3.8, average axial velocities (non-dimesnionalized wrt the local mean centerline values) are plotted against the transverse location (radial direction, non-dimensionalized wrt the local (1/e) velocity width). The values are taken from various axial locations in the region that is after the initial laminar state. All the points, lying on a Gaussian fit

(indicated by the dark red line) clearly shows that the flow has attained self-similarity after the initial 20-30 **d**.

The following were the simulation parameters corresponding to all the results presented for the viscosity ratio being unity:

Core-radius of the vortex blobs at the inlet: 0.25

Inlet pipe length: 50

Core radius beyond which vortex splitting is performed = 1

All the above three values are non-dimensionalized wrt the inlet slot width.

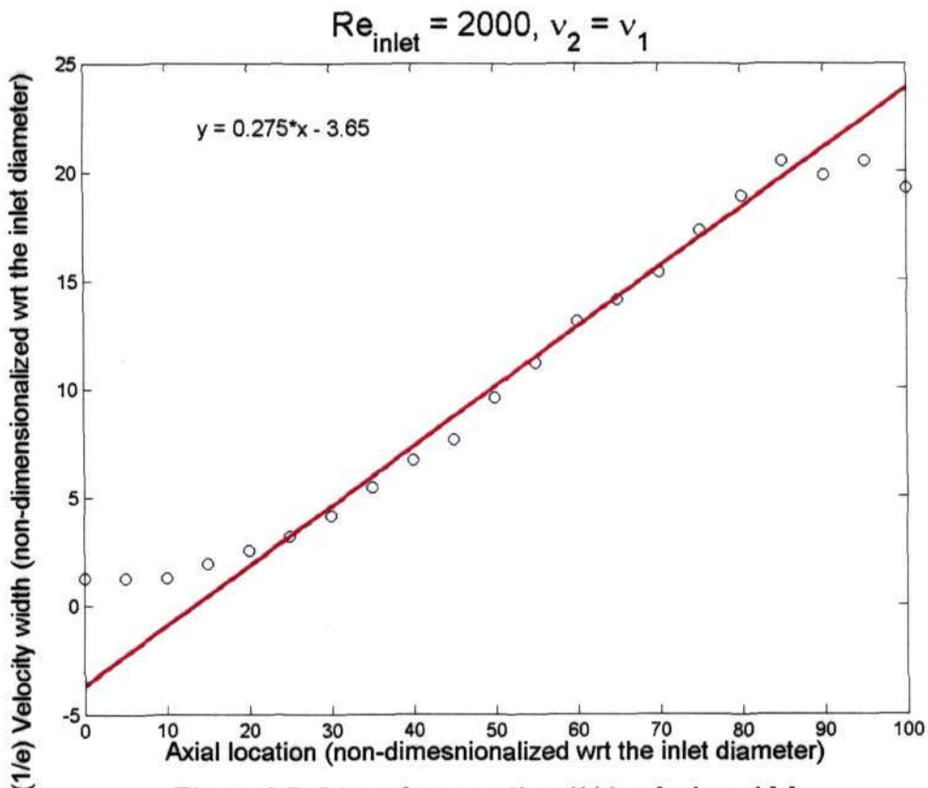

Figure 3.7: Linearly spreading (1/e) velocity width

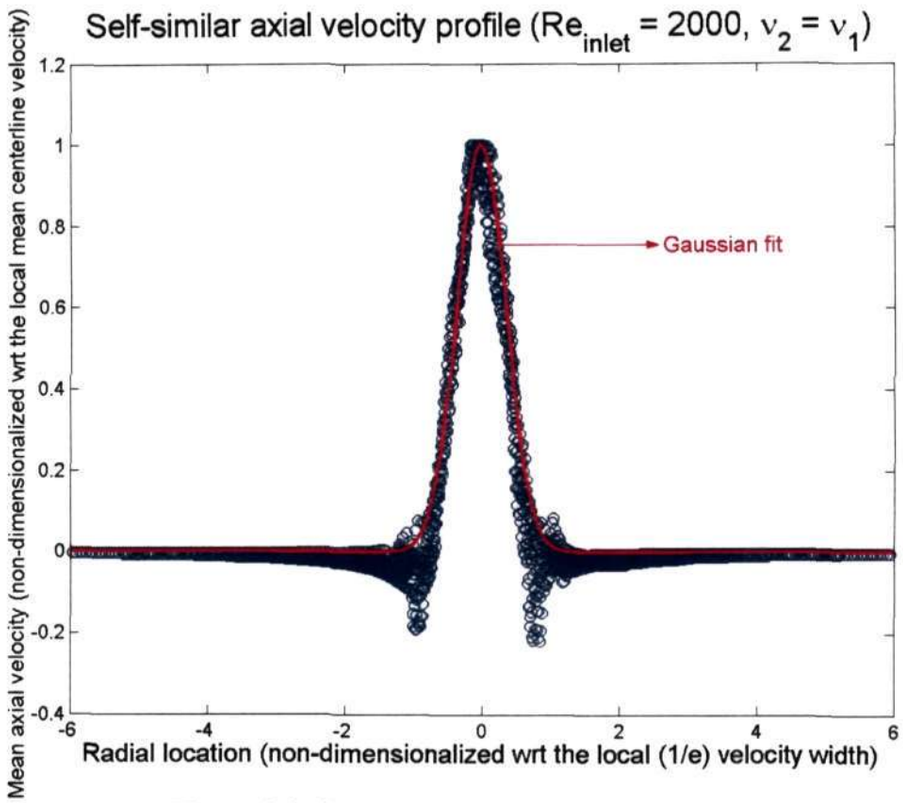

Figure 3.8: Self-similar axial velocity profile

We were interested in the distribution of the inlet fluid concentration in the case of the viscosity ratio being equal to unity also. Hence, we proceeded by doing the simulations for $\mathbf{Re_{inlet}}$ = 2000 and ν_2/ν_1 =1 with the scalar particles representing the inlet fluid. Averaging was performed over 200 time steps and the maximum core radius specified for the vortex blobs was slightly smaller than what was specified for the earlier case.

Figure 3.7 shows the plot of the variation of the (1/e) velocity width with axial distance. As noted earlier, the slope is very small in the initial laminar region and then becomes larger once the flow becomes turbulent. Figure 3.9 shows a plot of the (1/e) scalar width and the velocity width with axial distance. Interestingly, the scalar width turns out be larger than the velocity width at every axial location. It is interesting to note that the scalar width can be much smaller than the velocity width or can be comparable to it

depending on what the inlet Reynolds number and the viscosity ratio are. Both the scalar width and the velocity width are shown together in figure 3.9. The scalar spread rate being larger than the velocity spread rate in a fully turbulent jet is consistent with the results obtained by Fischer[10].

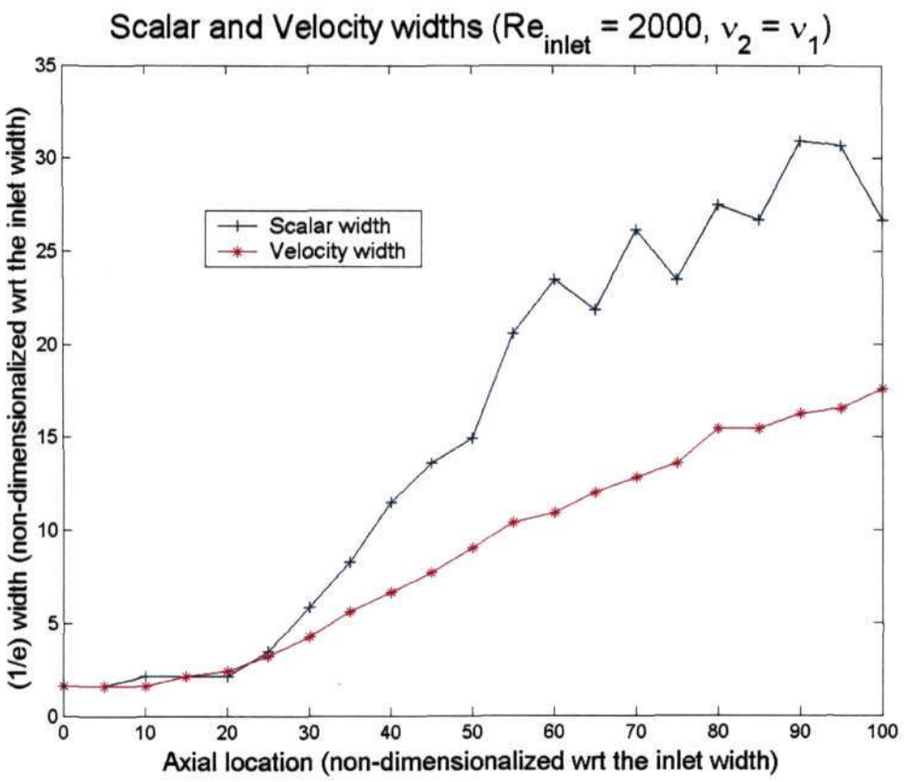

Figure 3.9: Scalar and Velocity widths

In figure 3.10, by plotting the mean axial velocity profile at different axial locations and collapsing them to a single Gaussian variation by using the appropriate velocity and length scales, the self-similarity of the velocity profile is shown. In figure 3.11, the variation of the mean centerline axial velocity with axial distance is plotted. As expected, it decreases with axial distance, the rate of decrease being smaller as we go further downstream.

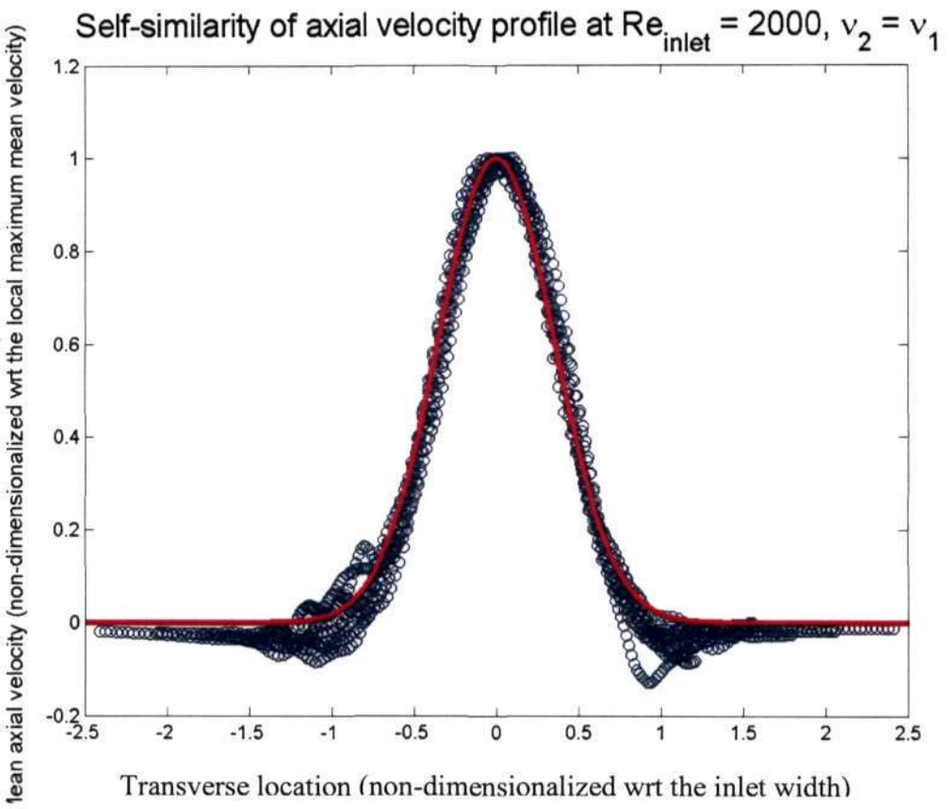

Figure 3.10: Self-similarity in the axial velocity profiles

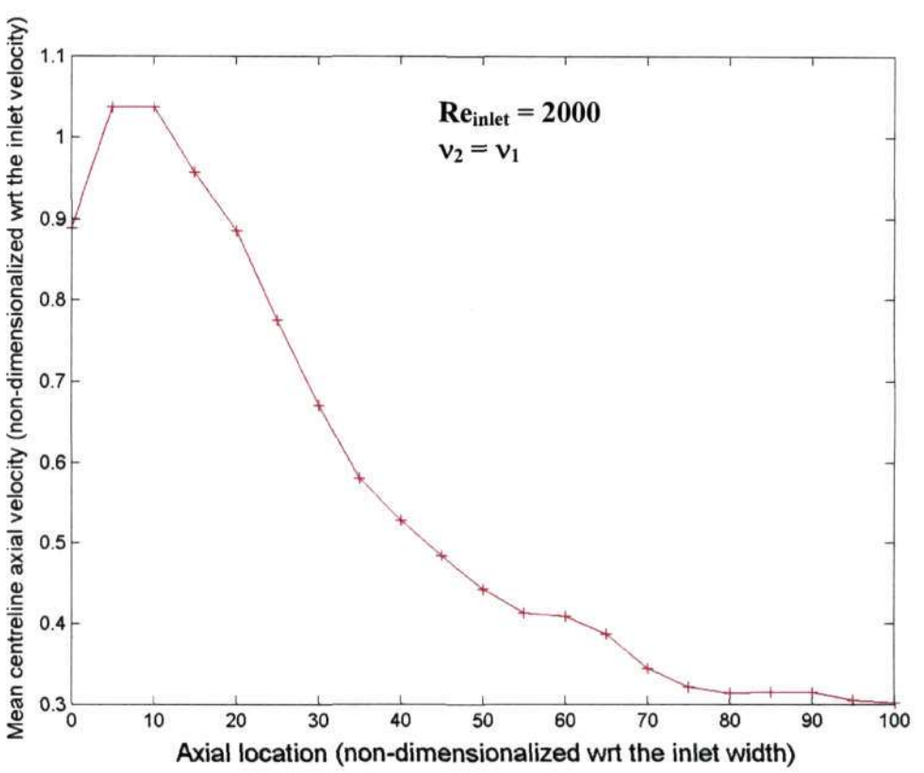

Figure 3.11: Centreline mean axial velocity Vs Axial distance

Figure 3.12 shows the variation of the mean inlet concentration, averaged over 200 time steps. Important to be noted is the fact that the scalar spread rate is appreciable, and traces of the inlet have spread to a fairly large extent. The scalar widths here are greater than the axial velocity widths. This qualitative trend of the scalar widths being greater than the velocity widths is always observed in fully turbulent jets. Instantaneous distributions of the inlet concentration and the vorticity are shown in the figures 3.13 and 3.14 respectively.

3.7.2 Viscosity Stratification

The simulations were extended to cases where the viscosity was non-uniform in space. The main issue here was the requirement of large computing power and time. To be able to capture the effects of the ambient viscosity clearly, we needed to go to a viscosity ratio that was as high as 100. Firstly, the number of scalar particles needed to represent the inlet fluid to a reasonably good extent was very large. The core radius of the scalar particles, in a way specifies the resolution in evaluating the concentration at each point. This, even if reasonably small, would lead to a number of particles that is at least twice that of the number of vortex blobs in the domain in the equal viscosity case. Secondly, if the maximum core size for the vortex blobs (which specifies the resolution in evaluating the vorticity at each point) is specified to be the same as that for the equal viscosity case, the number of vortex particles reaching this maximum value will be too many too soon. This results in at least a hundred-fold increase of the number of particles for the particular case of the viscosity ratio being 100. Based on the above issues, the following simulation parameters were used for the viscosity-stratified cases:

Core-radius of the vortex blobs at the inlet = 0.25
Inlet pipe length = 50
Core radius beyond which vortex splitting is performed = 7.5
Core radius of the concentration particles = 0.25

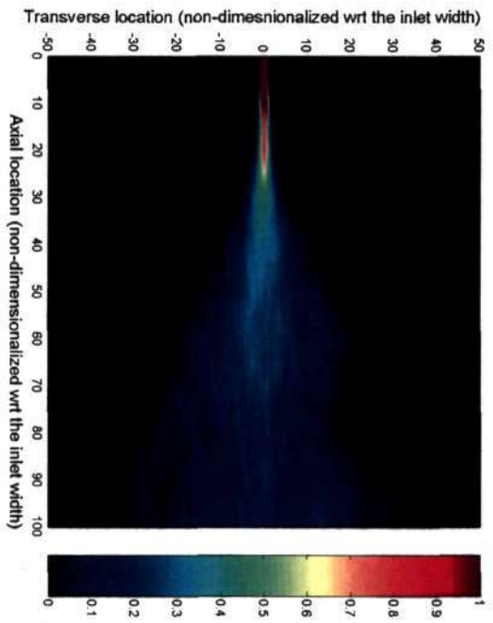

Figure 3.12: Average inlet fluid concentration ($Re_{inlet} = 2000$, $\nu_2 = \nu_1$)

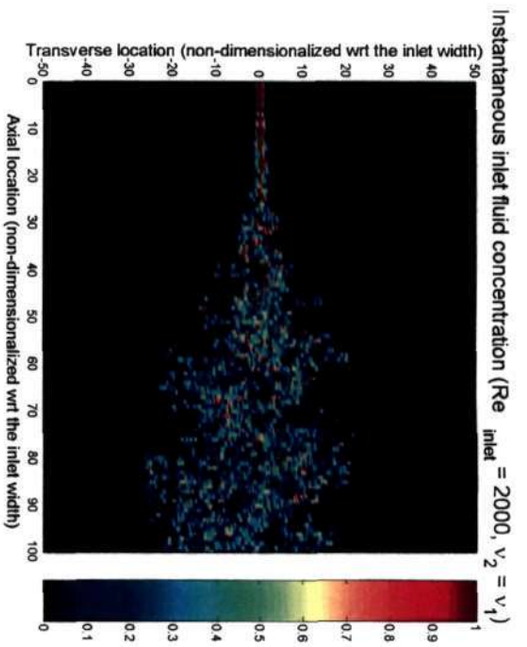

Figure 3.13: Instantaneous inlet fluid Concentration ($Re_{inlet} = 2000$, $\nu_2 = \nu_1$)

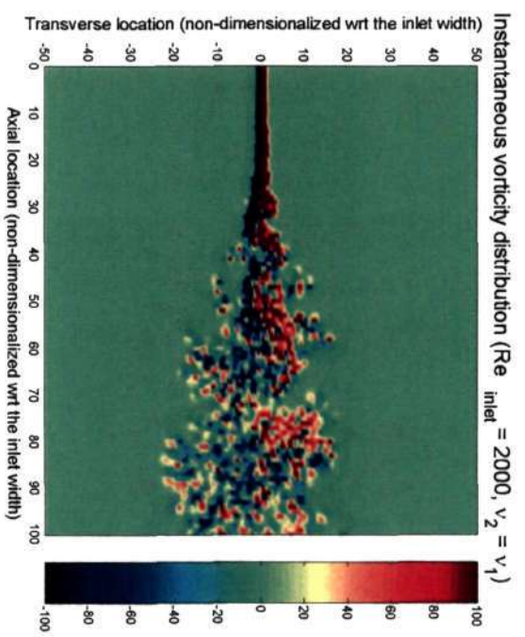

Figure 3.14: Instantaneous vorticity ($Re_{inlet} = 2000$, $\nu_2 = \nu_1$)

Even though, we strongly believe the higher viscosity ratio cases have to be addressed with a resolution that is a lot better than what is suggested above, an interesting result regarding the velocity and the scalar spreads was captured.

In figure 3.15, a plot of the velocity and the scalar widths with axial distance for an inlet Reynolds number of 100 and a viscosity ratio of 50 is shown. We can clearly see that the velocity spread is much more than that of the concentration (of the inlet fluid) beyond some axial distance. This is in strong agreement with our experimental results where we showed that the scalar spread is much less compared to the axial momentum spread when the flow is far from being fully turbulent. A similar result has been obtained for a case where the inlet Reynolds number was 2000 and the viscosity ratio 100. This is shown in figure 3.16.

Velocity width is evaluated as the radial location where the mean value of the axial velocity drops to (1/e) of the local centerline mean axial velocity. Scalar width is evaluated as the radial location where the mean concentration of the inlet fluid drops to (1/e) of the local centerline mean concentration.

The widths in figure 3.16 are larger than the corresponding values in figure 3.15 and this is consistent with the experimental observations where an increase in the inlet Reynolds number results in the increase in scalar widths for the same viscosity ratio. The effects of the change in the viscosity ratio from 50 to 100 are not as large as the increase in the inlet Reynolds number from 100 to 2000.

For the case corresponding to $Re_{inlet} = 100$ and $\nu_2 = 100\nu_1$, we have plotted the average velocity and scalar concentration profiles at different axial locations. These plots are shown in figures 3.17 and 3.18. The qualitative difference in the variations of the scalar concentration and the axial velocity are very evident. The axial velocity always has a long tail indicating that the axial momentum spreads to a larger extent than the scalar concentration. The red line shows the distribution of the scalar concentration and the blue line the axial velocity in both the figures.

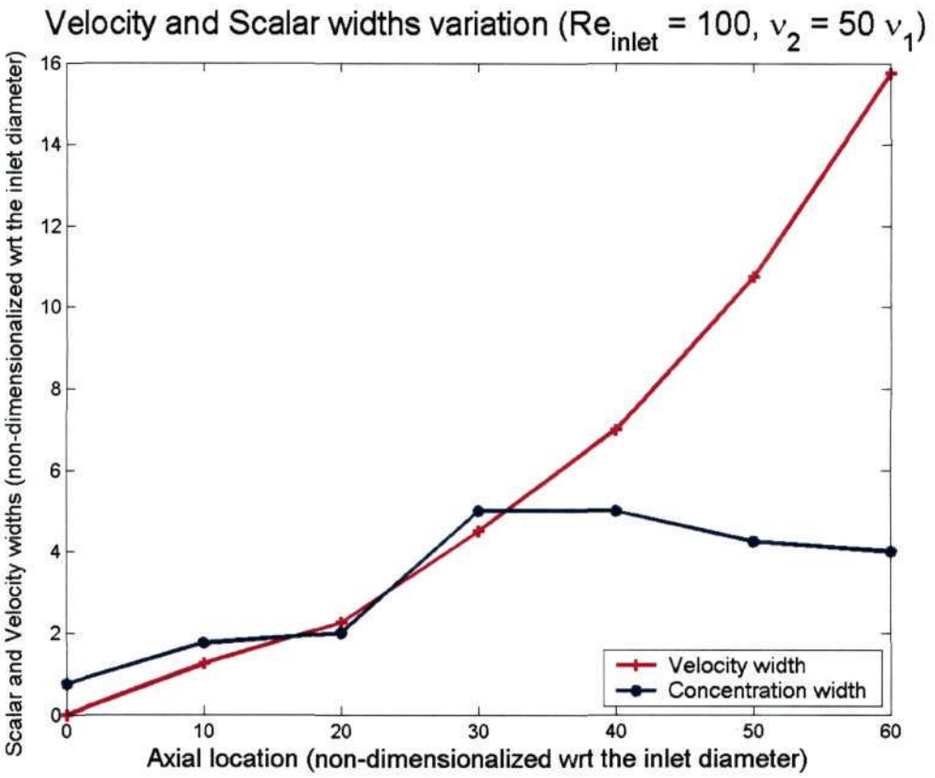

Figure 3.15: Velocity and Scalar widths

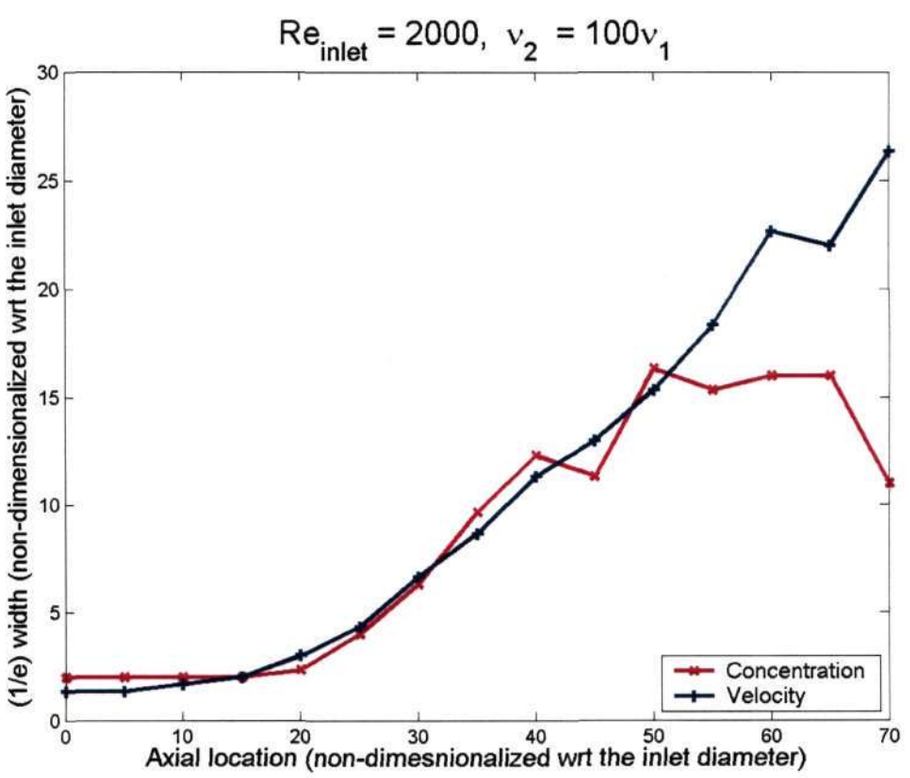

Figure 3.16: Velocity and Scalar widths

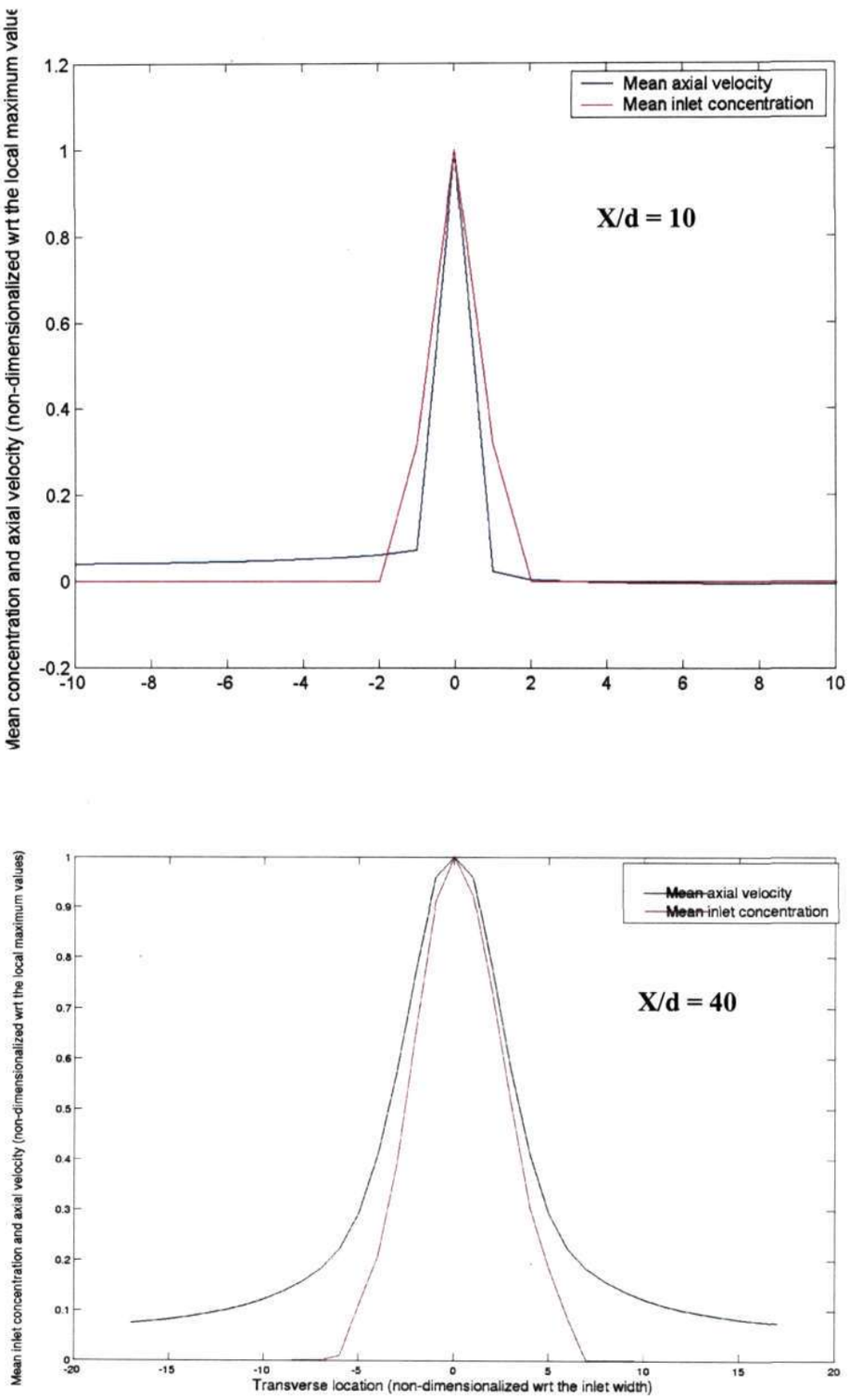

Figure 3.17: Scalar and Velocity widths, $Re_{inlet} = 100$, $\nu_2 = 100\nu_1$

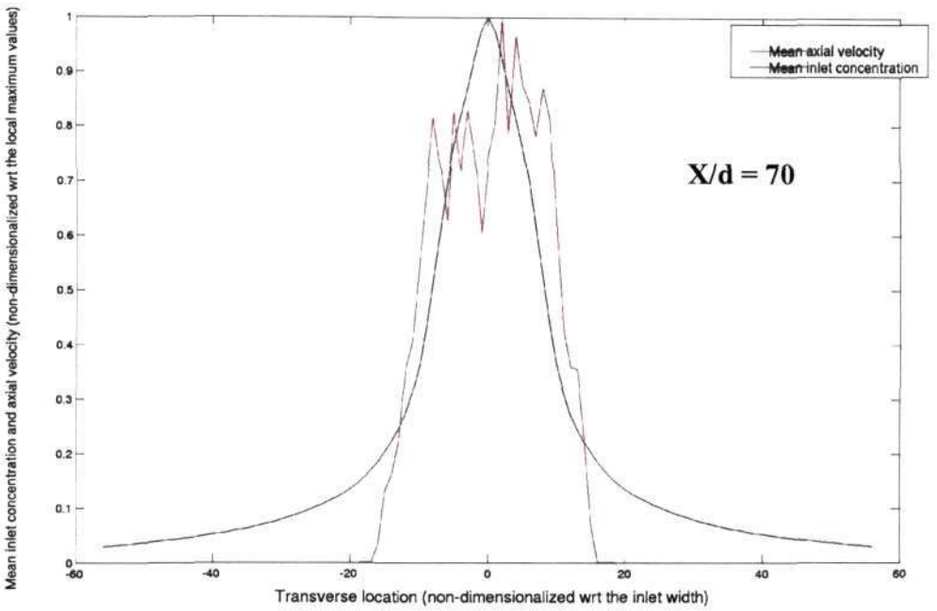

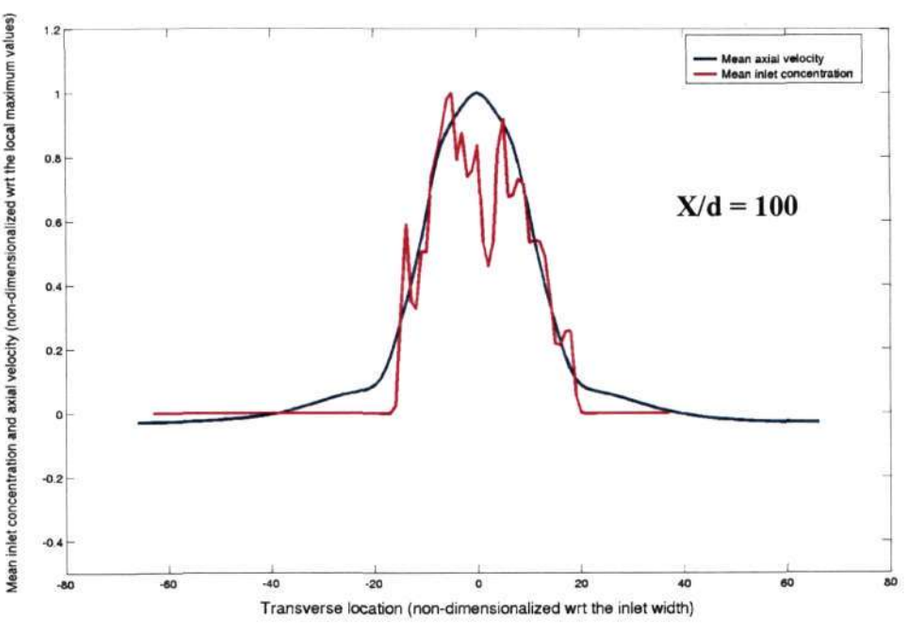

Figure 3.18: Scalar and Velocity widths, $Re_{inlet} = 100$, $\nu_2 = 100\nu_1$

Chapter 4

Discussion and Conclusions

The primary role of the viscosity of the ambient fluid in affecting the entrainment process in a buoyant jet has been identified.

For a given inlet Reynolds number, there exists a particular value for the viscosity ratio, beyond which the suppression in the entrainment in appreciable. Similarly, for a given viscosity ratio, there exists an inlet Reynolds number beyond which the suppression in the entrainment becomes negligible.

In all the cases, it has been observed that the entrainment is negligible in the initial laminar portion of the flow. Also, the presence of coherent structures seems to be well correlated with appreciable entrainment. To explain this, we look at the three basic steps involved in entrainment, as suggested by Roshko[37] and Dimotakis[38]. The process of entrainment in turbulent jets is understood to occur in three phases. The first step, known as the *induction* phase, involves the engulfment of ambient fluid driven by the Biot-Savart-induced velocity of large vortices residing at the edge of the jet. The inducted fluid, although still irrotational, forms a part of the moving turbulent fluid. Subsequent turbulent straining of the inducted fluid reduced its spatial scale to a small enough value at which viscous diffusion dominates (*diastrophy*). Finally, viscous diffusion enables the inducted fluid to mix at the molecular level with the turbulent flow (*infusion*). Any mechanism that interferes with any of the above three phases will affect the entrainment process.

Off-source buoyancy addition and axial acceleration inhibit the *induction phase* whereas high viscosity ambient suppresses both the *induction* and the *diastrophy phases*. Also, the induction phase is very ineffective in the initial laminar portion of a turbulent jet. Clustering of circulation, which indicates formation of coherent structures, is accompanied by an increase in entrainment in the turbulent region. The inlet laminar portion, represented by two parallel vortex sheets (resulting in no net vorticity at the axial

location) will induce no velocity in the ambient fluid and hence the induction phase is ineffective. Hence, the role of coherent structures in enhancing the induction process (and hence the entrainment process) is understood.

The ambient viscosity plays a key role in suppressing the formation of coherent structures. The longer wavelength waves remain even in the case of the entrainment being completely suppressed in a high-viscosity ambient medium.

As noted in the chapters 2 & 3, the difference between the scalar and the axial momentum spreads is more and more discernible as the flow moves away from the fully turbulent regime. We have shown by experiments, how the radially inward velocity observed in a jet/plume in a medium of the same viscosity, gradually changes to co-flowing axial velocity with increasing ambient viscosity. The axial momentum, spreading to a much larger extent than the scalar in the high-viscosity case is an important factor for understanding the 'entrainment' process. As we have already discussed, the high-viscosity ratio is a case where the mixing between the inlet and the ambient fluid has been completely suppressed but the axial momentum has spread to a large extent. Commenting on entrainment, purely based on the axial momentum spread is completely misleading. It is important to look at the concentration widths rather than the velocity widths in entrainment studies, as the former determines important dynamics like the combustion efficiency in flames and precipitation in clouds. Also, the concentration dilution represents the final step in the entrainment process, namely infusion.

Absence of coherent structures for a jet in high viscosity ambient fluid is due to the increased stability of the shear layers. Large velocity width of the jet in comparison to its small concentration width indicates moving away of the inflection point in the velocity profile from the region of high shear and this may contribute to the increased stability of the shear layers. Thus, relating shear layer instability to the entrainment process in free-shear flows will be helpful in modeling their behavior and can address the observed variation of entrainment coefficient in free-shear flows subjected to different body forces as suggested by [6].

Results from the simulations were very satisfactory for the case of the viscosity ratio being unity. Self-similarity and rapid entrainment were two primary features that were predicted for a turbulent jet in a medium of the same viscosity as the inlet fluid. The scalar width being around 40-50 % greater than the velocity width at any axial location (beyond the initial laminar region) in a 2-D planar jet was established. Extending the simulation scheme to viscosity-stratified case was non-trivial and the current scheme, which approximates the terms involving viscosity derivatives in the vorticity equation, demands large computing power. However, the main result of the axial momentum spreading more than the scalar in the case of a high-viscosity ambient medium was captured.

REFERENCES

[1] Morton B.R., Taylor G.I. and Turner J.S., "Turbulent gravitational convection from maintained and instantaneous sources", Proc. R. Soc. Lond. A **234**, 1-23 (1956)

[2] J.S.Turner, "Turbulent Entrainment: The development of the entrainment assumption and its application to geophysical flows", J. Fluid Mech. **173**, 431(1986)

[3] G.S. Bhat and R. Narasimha, "Volumetrically heated jet: Large eddy structure and entrainment characteristics", J. Fluid Mech. **329**, 303(1996)

[4] D.W. Choi, F.B. Gessner, and C.G. Oates, "Measurements of confined, coaxial jet mixing with pressure gradient", J. Fluids Engg., **108**, 39(1986)

[5] R. Narasimha and K.R. Sreenivasan, "Relaminarization of fluid flows", Adv. Appl. Mech., **19**, 221(1979)

[6] K.R. Sreenivas and Ajay K. Prasad, "Vortex-dynamics model for entrainment in jets and plumes", Phys. Fluids, **12(8)**, 2101(2000)

[7] E.J. Gutmark and F.F. Grinstein, "Flow control with non-circular jets", Ann. Rev. Fluid Mech., **31**, 239(1999)

[8] H. Campbell and J.S. Turner, "Turbulent mixing between fluids with different viscosities", Nature, **313**, 39(1985)

[9] J.S. Turner, "Buoyancy Effects in Fluids", Cambridge University Press, 367(1973)

[10] H.B. Fischer, E.J. List, R.C.Y. Koh, J. Imberger and N.H. Brooks, "Mixing in Inland and Coastal Waters", Academic, 483(1979)

[11] V.H. Chu, C. Senior and E.J. List, "Transition from a turbulent jet into a turbulent plume", ASME Conference, Boulder, Colorado, June 1981.

[12] G.K. Batchelor, "Heat convection and buoyancy effects in fluids", Q. J. R. Met. Soc. **80**, 339(1954)

[13] B.R. Morton, "Forced plumes", J. Fluid Mech., **5**, 151(1959)

[14] E. J. List and J. Imberger, "Turbulent entrainment in buoyant jets", Proc. ASCE, J. Hydraul. Div., **99**, 1461(1973)

[15] A.J. Basu and R. Narasimha, "Direct numerical simulation of turbulent flows with cloud-like off-source heating", J. Fluid Mech., **385**, 199(1999)

[16] L. Venkatakrishnan, G.S. Bhat, A. Prabhu and R. Narasimha, "Visualization studies

of cloud-like flows", Curr. Sci., **74**, 597(1988)

[17] R.L. Simpson and C.R. Shackleton, "Laminariscent turbulent boundary layers: Experiments on nozzle flows", Proj. SQUID Tech. Rep. No. SMU-2-PU (1977)

[18] Q. Zhang and H. Johari, "Effects of acceleration on turbulent jets", Phys. Fluids, **8**, 2185(1996)

[19] Manikandan M.S. and Sreenivas K.R., "Effects of ambient viscosity on the turbulent jet entrainment process", SRFP-2003 report, JNCASR, Bangalore.

[20] Debopam Das, Sreenivas K.R., Jayawant H. Arakeri and Srinivasan J, "On the bifurcation of laminar buoyant jets discharged horizontally", Proceedings of the third world conference on Experimental Heat Transfer, Fluid mechanics and Thermodynamics, pp 855-862, USA, 1993.

[21] Sreenivas K.R., "Study of entrainment process in a planar jet using diffusion-vortex method", Proceedings of The Tenth Asian Congress of Fluid Mechanics, B33, Peradeniya, Sri Lanka, 17-21 May 2004.

[22] Lorenal A. Barba, "Vortex Method for computing high-Reynolds number flows: Increased accuracy with a fully mesh-less formulation", PhD thesis, California Institute of Technology, 2004.

[23] Shankar Subramaniam, "A new mesh-free vortex method", PhD thesis, The Florida State University, 1996.

[24] Chorin A.J., "Numerical study of slightly viscous flow", J. Fluid Mech., **57**, 785(1973).

[25] Koumoutsakos, Leonard A. and Pepin F., "Boundary conditions for viscous vortex Methods", J. Comp. Phys., **113**, 52(1994).

[26] Beale J.T. and Majda A., "Rates of convergence for viscous splitting of the Navier-Stokes equations", Math. Comp., **37**, 243(1981).

[27] Ying L.A., "Viscous splitting for the unbounded problem of the Navier-Stokes equations", Math. Comp., **55**, 89(1990).

[28] Ogami Y. and Akamatsu T., "Viscous flow simulation using the discrete vortex model – The diffusion velocity method", Computers & Fluids, **19**, 433(1991).

[29] Kempka, S.N. and Strickland, J.H., "A method to simulate viscous diffusion of vorticity by convective transport of vortices at a non-solenoidal velocity" Sandia

Laboratory Report SAND93-1763, 1993.

[30] Kuwahara K. and Takami H., "Numerical studies of two-dimensional vortex motion by a system of points", J. Phys. Soc. Japan, **34**, 247(1973).

[31] Greengard C., "The core spreading vortex method approximates the wrong equation", J. Comp. Phys., **61**, 345(1985).

[32] Rossi L.F., "Resurrecting core spreading vortex methods: A new scheme that is both deterministic and convergent", SIAM J. Sci. Comput., **17**, 370(1996).

[33] Leonard A., "Vortex methods for flow simulation", J. Comp. Phys., **37**, 289(1980).

[34] Batchelor G.K., "An Introduction to Fluid Dynamics", Cambridge University Press, 1967.

[35] Rossi L.F., "Merging computational elements in vortex simulations", SIAM J. Sci. Comput., **18**, 1014(1997).

[36] Clarke N.R. and Tutty O.R., "Construction and validation of a discrete vortex method for the two-dimensional incompressible Navier-Stokes equations", Computers & Fluids, **23**, 751(1994).

[37] Roshko A., "Structure of turbulent shear flows: a new look", AIAA J., **14**, 1349-1357(1976).

[38] Dimotakis P.E., "Two-dimensional shear-layer entrainment", AIAA J., **24**, 1791-1796(1986).

[39] Agarwal A. and Prasad A.K., "Evolution of a turbulent jet subjected to volumetric heating", J. Fluid Mech., **511**, 95(2004).